이학박사 학위논문

Electrical Properties of Sorted Carbon Nanotube Networks and Their Application for Gas Sensors

분리된 탄소나노튜브의 전기적 성질과 이를 이용한 가스센서 개발에 관한 연구

2017년 7월

서울대학교 대학원

물리·천문 학부

김 정 수

Electrical Properties of Sorted Carbon Nanotube Networks and Their Application for Gas Sensors

Jeongsu Kim

Supervised by
Professor Seunghun Hong

A Dissertation Submitted to the Faculty of
Seoul National University
in Partial Fulfillment of the Requirements for the Degree of
Doctor of Philosophy

July 2017

Department of Physics and Astronomy
Graduate School
Seoul National University

Abstract

Electrical Properties of Sorted Carbon Nanotubes and Their Application for Gas Sensor

Jeongsu Kim
Department of Physics and Astronomy
The Graduate School
Seoul National University

Carbon nanotube (CNT) is considered as a promising material for future electronics due to its excellent electrical properties such as a high current density, a high on-off ratio, a high mobility and a low subthershold swing. However, practical applications for CNT-based devices are hindered by complex and time-consuming fabrication processes. For example, the chirality of an as-grown CNT is determined randomly, so As-grown CNTs has the problem that they consist of semiconducting CNTs (s-CNTs) and metallic CNTs (m-CNTs). The electrical properties of s-CNTs and m-CNTs are opposite to each other. Thus, it is difficult to expect a good performance when a device is made using as-grown CNTs. To solve the problem, recently, a “density gradient ultracentrifugation (DGU)” method was developed to sort as-grown CNTs into m-CNTs and s-CNTs. However, practical applications

using sorted-CNTs are still being studied because of the complexity of the fabrication process.

In this dissertation, I and co-works have explored electrical properties of sorted CNTs. In addition, we will propose a new strategy for the fabrication of CNT-based gas sensors as a practical application.

First, we will discuss pristine semiconducting carbon nanotube network-based devices exhibiting intrinsic characteristics. Conventional sorted CNT-based devices have disadvantages that surfactants or CNT bundles are exist in their channels. These surfactants and CNT bundles lower the performance of the performance of CNT-based devices, but it is extremely difficult to remove both surfactants and CNT bundles simultaneously. Here, the solutions of pristine s-CNT without bundles or organic impurities were prepared in 1, 2-dichlobenzene solutions via filtration and centrifugation processes. A FET device based on a pristine s-CNT network exhibited a rather large on−off ratio up to over $\sim 10^6$ and a subthreshold swing as small as $\sim$490 mV/dec, which are comparable to those of devices based on a single s-CNT.

Next, we will discuss the scanning noise microscopy method for the measurement of the noise characteristics of sorted carbon nanotube networks. Here, we measured the current maps and the electrical noise power spectral density (PSD) maps of a s-CNT network and a m-CNT networks via a modified conducting AFM system. By analysing the current maps and the PSD maps, we investigated the noise source activities of sorted CNTs. We found that the noise activities of sorted CNT

networks were just depending on the diameter of each CNT and the density of CNT network. Also, in the case of a s-CNT network, we found that noise activities were high at crossed-CNT junctions.

Lastly, a dye-functionalized sol-gel matrix on a s-CNT network for dual-mode sensing will be discussed. Here, the CNT-dye hybrid gas sensors were fabricated by functionalizing dye molecules on top of s-CNT networks via a sol-gel method. The CNT-dye hybrid gas sensors could selectively detected SO_2, NH_3 and Cl_2 gases. The sensitivity of the gas sensor exhibited more than 50 % by the exposure to the gas species with its concentration even under its permissible exposure limit. Also, we could refresh used gas sensors simply by exposing it to fresh N_2 gas without any heat treatment.

These works could provide an important insight regarding the electrical properties of sorted CNTs and their possibility for practical applications.

Keywords:

Carbon nanotube, Transistor, Centrifugation, Atomic force microscopy, Low-frequency noise, Noise imaging, Colorimetric sensor, Gas sensor

Student Number: 2013-30112

Contents

List of Figures

Chapter 1.
Introduction

1.1 Carbon Nanotubes

Carbon nanotubes (CNTs) are one of carbon allotropes such as graphene, diamond, graphite and fullerene. The structure of a carbon nanotube is a sheet of a graphene rolled up into a cylinder (Fig. 1.1) [1]. The length-to-diameter ratio of a CNT is up to 28,000,000 times [2]. Despite this unique structure, the tensile strength of a CNT is extremely strong because a CNT is constituted by covalent sp2-bonded carbon atoms, which are stronger than sp3 bonds. Also, CNTs have excellent characteristics in terms of their thermal conductivities, high conductivities, high carrier densities and ballistic transport. Thus, CNTs are widely studied in various fields such as nanoelectronic devices, solar cells, energy storage devices and sensors.

CNTs can be classified into single-walled CNTs (swCNTs) and multi-walled CNTs (including double-walled CNTs) depending on the number of rolled graphene sheets. The diameters of single-walled CNTs are about 0.6~2.0 nm and the diameters of multi-walled CNTs are about 5 ~ 100 nm. Here, the electrical properties and diameters of a single-walled CNT are

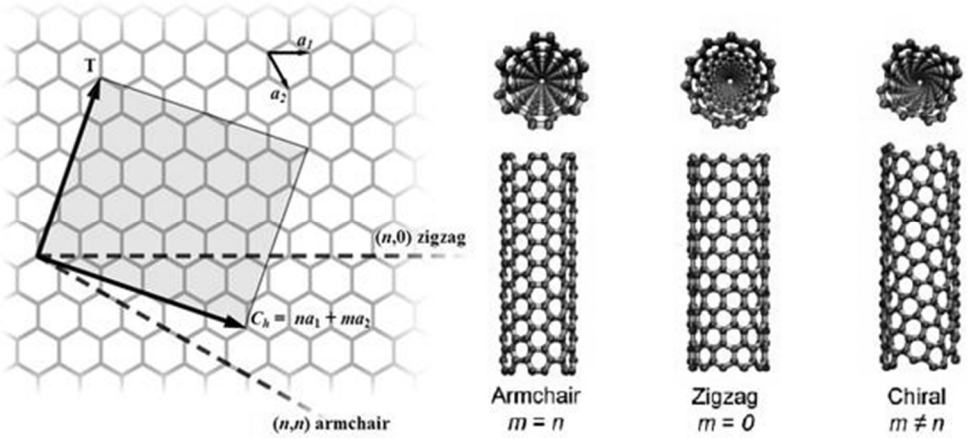

Fig 1. 1 The structure of a carbon nanotube [1].

determined by a chiral vector of a single-walled CNT. Fig. 1.1 shows unit vectors and a chiral vector of a CNT expressed on a graphene sheet. Here, a vector $\boldsymbol{T}$ represents the direction of a CNT and is called the translational vector of a CNT. Also, a vector $\boldsymbol{C_h}$ represents the direction of a CNT and is called the chiral vector of a CNT. Unit vectors of a graphene sheet are denoted by $\mathbf{a_1}$ and $\mathbf{a_2}$. Using the unit vectors, we can describe a $\boldsymbol{C_h}$ by

$$\boldsymbol{C_h} = n\mathbf{a_1} + m\mathbf{a_2} \equiv (n, m), \quad (n, m \text{ are integer}, 0 \leq m \leq n) \quad \text{(Eq. 1. 1)}$$

If a chiral vector of a carbon nanotube satisfies $n = m$, the carbon nanotube is called an armchair tube. Also, if a chiral vector of a carbon nanotube satisfies $m = 0$, the carbon nanotube is called a zigzag tube. The radius of a carbon

nanotube with any chiral vector is described by

$$d_t = \frac{\sqrt{3}a_{C-C}}{\pi}\sqrt{n^2 + m^2 + nm} = \frac{|\vec{C}|}{\pi} \qquad \text{(Eq. 1. 2)}$$

Here, $\boldsymbol{a_{c\text{-}c}}$ ($\sqrt{3}$ · 0.144 nm = 0.249 nm) is called the lattice constant of a graphene sheet. A angle between a chiral vector of a CNT and the zigzeg chiral vector is called a chiral angle and described by

$$\cos\theta = \frac{C_h \cdot a_1}{|C_h||a_1|} = \left(\frac{2n + m}{2\sqrt{n^2 + m^2 + nm}}\right) \qquad \text{(Eq. 1. 3)}$$

The energy band structure of a carbon nanotube can be calculated by adding the azimuthal periodic boundary condition on the energy band structure of a graphene sheet. First, the energy band structure of a graphene sheet is calculated by nearest neighbor thigh binding approximation (Eq. 1. 4) [3].

$$E(k) = \pm t\sqrt{1 + 4\cos(\frac{a_{c-c}k_y}{2})\cos(\frac{\sqrt{3}a_{c-c}k_x}{2}) + 4\cos^2(\frac{a_{c-c}k_y}{2})} \qquad \text{(Eq. 1. 4)}$$

Here, $\boldsymbol{t}$ (-2.72 eV) is the tight binding overlap energy of a C-C bond. To calculate the energy band structure of a carbon nanotube, we have to add the boundary condition of the equation (Eq. 1.5) on the equation (Eq. 1. 4).

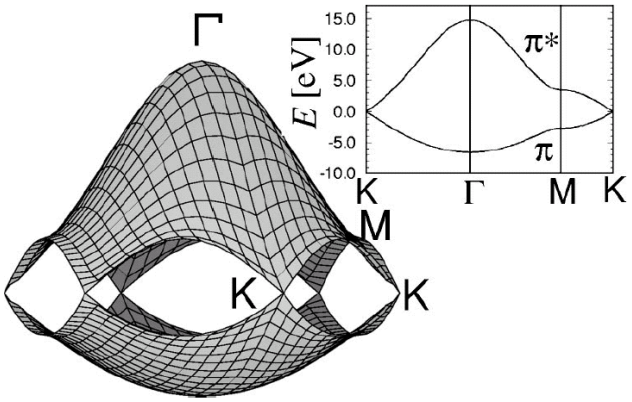

Fig 1. 2 The energy band structure of a graphene [4]

$$k \cdot C_h = k_x \frac{\sqrt{3}}{2} a_{c-c}(n+m) + k_y \frac{a_{c-c}}{2}(n-m) = 2\pi q \qquad \text{(Eq. 1. 5)}$$

Here, q is an integer. This boundary condition indicates that the wave function of a CNT returns its original wave function when rotated by 2π along the vector T axis. Among the energy levels of a graphene, the energy levels satisfying the equation (Eq. 1. 5) become the permissible energy levels of a CNT with a specific chiral vector C_h. If the chiral vector of a CNT satisfies that the lines satisfying the equation (Eq. 1. 5) pass through the Brillouin zone of the graphene such as Fig 1.3, the CNT shows metallic behavior because the band gab of the CNT is zero.

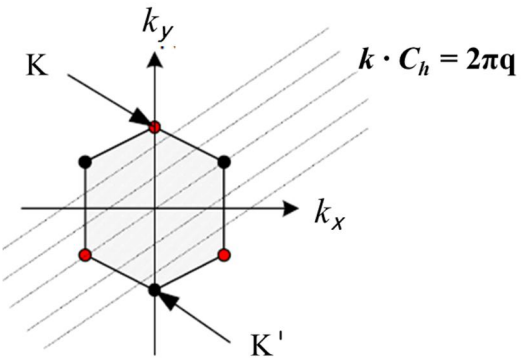

Fig 1. 3 Brillouin zones of a graphene and $k \cdot C_h = 2\pi q$ lines [5].

The coordinates of vertexes of Brillouin zone is given by

$$\left(0, \pm\frac{4\pi}{3a_{c-c}}\right), \left(\frac{2\sqrt{3}\pi}{3a_{c-c}}, \pm\frac{2\pi}{3a_{c-c}}\right), \left(-\frac{2\sqrt{3}\pi}{3a_{c-c}}, \pm\frac{2\pi}{3a_{c-c}}\right) \quad (1.6)$$

Substituting these six coordinates into the equation (Eq 1. 5) gives a following relationship.

$$k \cdot C_h = 0 \cdot (n+m) + \frac{2\pi}{3}(n-m) = 2\pi q \qquad \Rightarrow \qquad (n-m) = 3q \quad (1.7)$$

The relation means that there's no band gab when the chiral vector of a CNT satisfying the relation $(n - m) = 3q$. Note that, one-third of as-grown CNTs are metallic because chiral vectors of the CNTs are randomly determined.

1.2 Sorted Carbon Nanotubes

Since the discovery of CNTs, CNTs have been considered as

important materials for future electronics research due to their excellent characteristics in terms of their high carrier density, high transparency, high flexibility, low dimension and high tensile strength [6-14]. However, a new problem has arisen as the method for growing CNTs has been studied. Generally, researchers produce CNTs using furnaces. Here, during the production process, researchers cannot control the chiral vectors of the CNTs to be produced. Thus, as-grown CNTs are constituted by metallic CNTs and semiconducting CNTs in a ratio of 1 to 2. Both metallic and semiconducting CNTs have opposite electrical properties. Therefore, practical applications for CNT-based devices are difficult even though both CNTs have excellent characteristics. Recently, Hersam group developed a density gradient ultracentrifugation method to sort m-CNTs and s-CNTs from as-grown CNTs [15]. The method allows us to fabricate CNT-based devices using sorted CNTs.

Semiconducting CNTs are expected as good materials for semiconductor devices. S-CNT-based devices showed a high on-off ratio up to 10^6 [16], a high-mobility up to 100,000 $cm^2/V{\cdot}s$ [17, 18], a high-current density up to 4 x 10^9 A/cm^2 [19] and a low-subthreshold swing below 100 mV/dec [20-22]. Thus, it was expected that the s-CNT-based devices can apply for the fabrication of transistors, solar cells and chemical sensors.

Metallic CNTs are expected as good materials for nanoelectrodes. M-CNTs are useful for the applications of nanoelectrodes because of the low dimension of CNTs itself. Also, the high-transparency and the high-flexibility of m-CNTs allow us for the application of flexible and transparent nanoelectrodes [23, 24]. Additionally, m-CNTs have good thermal conductivities and can be used as a heat sink for nano devices [25].

With the advent of the CNT separation method, many researchers expected that the commercialization of CNT-based devices would be possible soon. However, the commercialization has not been done yet due to the subtitle of manufacturing method using CNTs.

References

[1] R. Saito, G. Dresselhaus and M. S. Dresselhaus, Physical Properties of Carbon Nanotubes, *Imperial College Press* (1998).

[2] L. X. Zheng et al., Ultralong single-wall carbon nanotubes. *Nat. Mater.* **3**, 673-676 (2004).

[3] J. A. Daggett, Theoretical Investigation of Carbon Nanotube Devices for Millimeter/Submillimeter Wave Analog Circuits, *Montana State University* (2009).

[4] R. Saito, G. Dresselhaus, M. S. Dresselhaus, Trigonal warping effect of carbon nanotubes. *Phys. Rev. B* **61**, 2981-2990 (2000).

[5] S. Datta, Quantum Transport: Atom to Transistor. *Cambridge University Press*, (2006).

[6] S. Iijima, T. Ichihashi, Single-Shell Carbon Nanotubes of 1-Nm Diameter. *Nature* **363**, 603-605 (1993).

[7] E. S. Snow, J. P. Novak, P. M. Campbell, D. Park, Random networks of carbon nanotubes as an electronic material. *Appl. Phys. Lett.* **82**, 2145-2147 (2003).

[8] E. Bekyarova et al., Electronic properties of single-walled carbon nanotube networks. *J. Am. Chem. Soc.* **127**, 5990-5995 (2005).

[9] C. Kocabas, M. A. Meitl, A. Gaur, M. Shim, J. A. Rogers, Aligned Arrays of single-walled carbon nanotubes generated from random networks by orientationally selective laser ablation. *Nano Lett.* **4**, 2421-2426 (2004).

[10] A. Behnam, A. Ural, Computational study of geometry-dependent resistivity scaling in single-walled carbon nanotube films. *Phys. Rev. B* **75**, (2007).

[11] F. M. Du, J. E. Fischer, K. I. Winey, Effect of nanotube alignment on percolation conductivity in carbon nanotube/polymer composites. *Phys. Rev. B* **72**, (2005).

[12] S. Kumar, J. Y. Murthy, M. A. Alam, Percolating conduction in finite nanotube networks. Phys Rev Lett 95, (2005).

[13] L. Hu, D. S. Hecht, G. Gruner, Percolation in transparent and conducting carbon nanotube networks. Nano Lett 4, 2513-2517 (2004).

[14] C. Kocabas et al., Experimental and theoretical studies of transport through large scale, partially aligned arrays of single-walled carbon nanotubes in thin film type transistors. Nano Lett 7, 1195-1202 (2007).

[15] M. S. Arnold, A. A. Green, J. F. Hulvat, S. I. Stupp, M. C. Hersam, Sorting carbon

nanotubes by electronic structure using density differentiation. Nat Nanotechnol 1, 60-65 (2006).

[16] A. Javey, J. Guo, Q. Wang, M. Lundstrom, H. J. Dai, Ballistic carbon nanotube field-effect transistors. Nature 424, 654-657 (2003).

[17] X. S. Wang et al., Fabrication of Ultralong and Electrically Uniform Single-Walled Carbon Nanotubes on Clean Substrates. Nano Lett 9, 3137-3141 (2009).

[18] T. Durkop, S. A. Getty, E. Cobas, M. S. Fuhrer, Extraordinary mobility in semiconducting carbon nanotubes. Nano Lett 4, 35-39 (2004).

[19] S. Hong, S. Myung, Nanotube electronics - A flexible approach to mobility. Nat Nanotechnol 2, 207-208 (2007).

[20] R. V. Seidel et al., Sub-20 nm short channel carbon nanotube transistors. Nano Lett 5, 147-150 (2005).

[21] A. Javey et al., High-kappa dielectrics for advanced carbon-nanotube transistors and logic gates. Nat Mater 1, 241-246 (2002).

[22] Z. X. Wang et al., Growth and Performance of Yttrium Oxide as an Ideal High-kappa Gate Dielectric for Carbon-Based Electronics. Nano Lett 10, 2024-2030 (2010).

[23] E. J. Spadafora et al., Work function tuning for flexible transparent electrodes based on functionalized metallic single walled carbon nanotubes. Carbon 50, 3459-3464 (2012).

[24] F. S. Lu, M. J. Meziani, L. Cao, Y. P. Sun, Separated Metallic and Semiconducting Single-Walled Carbon Nanotubes: Opportunities in Transparent Electrodes and Beyond. Langmuir 27, 4339-4350 (2011).

[25] C. Subramaniam et al., Carbon nanotube-copper exhibiting metal-like thermal conductivity and silicon-like thermal expansion for efficient cooling of electronics. Nanoscale 6, 2669-2674 (2014).

Chapter 2.
Pristine Semiconducting Carbon Nanotube Network Exhibiting Intrinsic Characteristics

2.1 Introduction

A field effect transistor (FET) based on a single semiconducting carbon nanotube (s-CNT) has been extensively studied due to its superior device characteristics such as a high current density [1], a high on−off ratio [2], a high mobility [3], and a low subthreshold swing [2, 4-6]. However, the complex and time-consuming fabrication processes for such single s-CNT-based FETs have hindered their practical applications. One solution for this problem can be a device based on s-CNT networks [7-16]. Various methods have been developed to achieve carbon nanotube materials with more than 99% of s-CNTs. However, previous device fabrication processes for FETs based on s-CNT networks often introduced various defects to the s-CNT networks, which could degrade the device performance. For example, surfactant molecules have been often utilized to prepare a well-dispersed s-CNT solution without bundles so that one can purify and deposit s-CNT

networks onto solid substrate. However, the residual surfactant molecules in the fabricated devices can degrade the device performance. Although the surfactant can be removed via various methods such as vacuum filtration and extensive rinsing, the removal of surfactant often increases the formation of CNT bundles in the networks. Since CNT bundles including metallic CNTs work as a metallic component, the formation of bundles, in effect, increases the ratio of metallic paths and results in a rather poor on−off ratio of the fabricated FET devices [9, 12, 13]. However, it has been extremely difficult to remove both surfactant molecules and CNT bundles from s-CNT network channels during previous device fabrication processes, which has been limiting the performance of fabricated FET devices.

Herein, we report a method for the large-scale fabrication of high-performance FETs based on pristine s-CNT networks without bundles or organic impurities, thus exhibiting its intrinsic characteristics. In this method, the solution of pristine s-CNTs without surfactant or CNT bundles were prepared in a nonpolar solvent via filtration and centrifugation processes, and molecular patterns on solid substrates were utilized to direct the adsorption of the s-CNTs onto specific regions on the substrates. Using this method, we could successfully fabricate the large scale patterns of s-CNT networks without organic contaminants or CNT bundles. FET devices based on such s-CNT networks exhibited a rather large on−off ratio up to over $\sim 10^6$ and a

subthreshold swing as small as ~490 mV/dec, which are comparable to those of devices based on a single s-CNT with the same device structures. Significantly, the s-CNT devices exhibited anomalous gating behaviors such as an on-current saturation at a large gate bias and unconventional scaling behaviors, which are quite different from those of previous s-CNT network-based devices. Such anomalous behaviors can be explained by a simple model based on the series networks of contact and s-CNT resistances, implying that these anomalous behaviors are, as a matter of fact, the intrinsic characteristics of pristine s-CNT network-based devices. Our work reveals a new insight about the intrinsic characteristics of pristine s-CNT network-based devices and, thus, should provide an important guideline for the future research and applications of s-CNT network-based devices.

2.2 CNT Schottky Barrier Transistor

Carbon Nanotube FETs operate as unconventional “Schottky barrier transistors”, in which switching occurs primarily by modulation of the contact resistance rather than the channel conductance. Fig. 2.1 shows the band bending in a three-terminal CNT device qualitatively for two

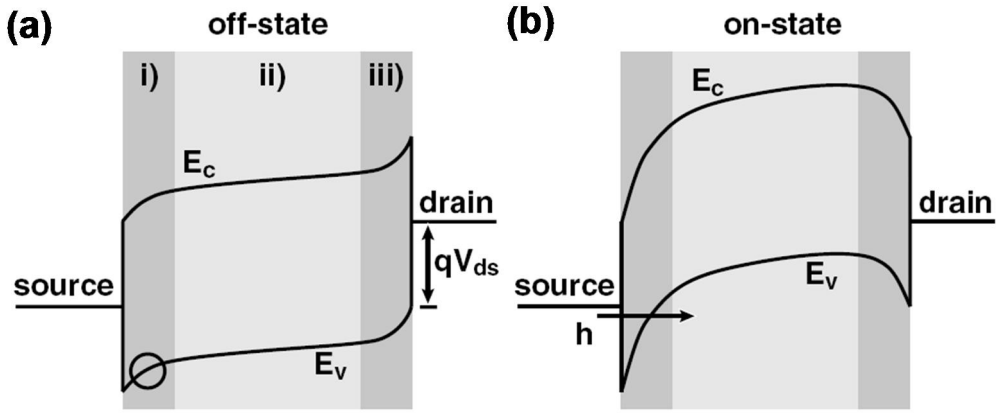

Fig. 2. 1 Qualitative response of the nanotube conduction and valence band on the gate voltage for a fixed negative source-drain voltage (a) A gate voltage below threshold voltage describing the situation in the transistor off-state. (b) The band bending situation for a gate voltage well above V_{th} [6].

different gate field conditions [6]. In case Fig. 2.1 (a), the device is essentially off -there is no charge accumulated on the CNT. In Fig. 2.1 (b), the gate voltage is sufficiently large to turn the transistor on. Since hole transport is considered, the important part to focus on is the valence band and here, in particular, the source side as emphasized by the circle in Fig. 2.1 (a). For discussion purposes, we divide the transistor into three segments. (i) and (iii) describe the situation close to source and drain, respectively, while (ii) accounts for the bulk part of the CNT. The most important ingredients are the Schottky barriers in (i) and (iii). The existence of these barriers at a CNT-metal interface has been reported before [17], and their critical role for the transport in a CNT field effect transistor is clarified here.

2.3 “Surface Programmed Assembly” Method

Recently, nanowire (NW) or carbon nanotube-based devices are widely studied to overcome the limitation of bulk silicon-based devices. These NW or CNT-based devices have excellent electrical properties compere to conventional Si-based devices. For example, a carrier density and a mobility of a CNT-based device are higher than conventional Si-based devices about 100 times and 1,000,000 times, respectively. Also, most of NW/CNT-based devices offer greater flexibilities compere to conventional Si-based devices.

However, NW or CNT-based devices have problems that the fabrication processes of the devices are complicate and time-consuming. Most of NW or CNT based-devices are fabricated by utilizing NTs or CNTs in solutions or powder form [18]. Therefore, we have to pick up and assemble individual NWs or CNTs to fabricate the devices on specific areas. Let’s assume that the manufacturing time of individual NW-based device is one second. Then, it will take about 30 years to build a single integrated circuit chip such as random-access-memory (RAM). Actually the manufacturing time of NW-based device often takes more than one day.

This type of problem is widely known as “nanomanufactoring”

problem. This problem has been holding back the practical applications of NW or CNT-based devices.

The self-assembly strategy can be applied to nanomanufacturing of hybrid devices through the new process called "surface-programmed assembly (SPA)" process (Fig. 2. 2) [19]. This process is comprised of two simple steps: 1) surface molecular patterning and 2) surface-directed assembly. First, the substrate is functionalized via specific chemical or biological functional groups such as carboxylic acid, amine, etc. The surface functionalization can be done by patterning molecular monolayer using various patterning method such as dip-pen nanolithography [20-24], microcontact printing [25-27], photo-lithography [28], etc. By patterning nanoscale regions of the substrate with specific functional groups, we are giving the solid substrate a capability to recognize specific nanostructures in the solution. When the patterned substrate is placed in the solution of nanostructures, the patterned regions have an affinity to specific nanostructures, and nanostructures are adsorbed onto the regions. This is actually very similar to our experience in an art class when we were in elementary school. When we draw a picture with glue on paper and throw sand particles on it, sand particles adhere only to the regions coated with glue. This phenomenon is often called "selective adsorption." The SPA process is somewhat similar to this practice in nanoscale. However, it also should be

noted that actual SPA process includes a bit more complicated mechanisms than simple selective adsorption. Presumably, the adhesion force between CNTs and polar molecular self-assembled monolayer (SAM) might be dipole-induced dipole interaction.

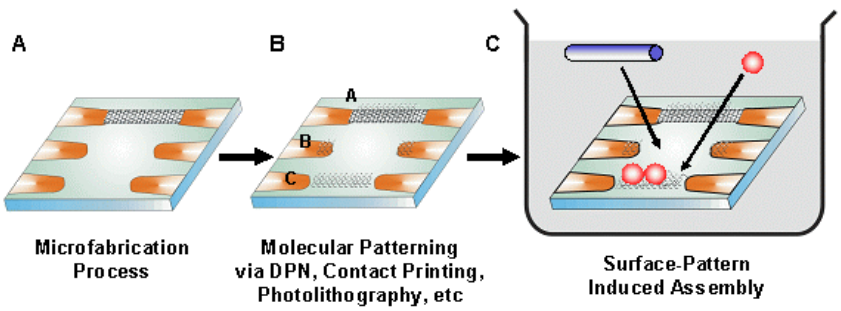

Fig. 2. 2 Diagram of surface programmed assembly

2.4 Experimental Procedure

2.4.1 Preparation of Pristine s-CNT Solution without Surfactant or CNT Bundles.

For the device fabrication, we utilized commercial surfactant-wrapped semiconducting CNTs (NanoIntegris Inc., purity ~99%, average diameter ~1.2 nm). Although the carbon nanotube materials contained more than 99% of semiconducting CNTs, previous device fabrication processes have often introduced various impurities (e.g., surfactant, CNT bundles) to the CNT network channel, which may degrade the device

performance [14, 15]. Fig. 2. 3 shows a schematic diagram depicting the fabrication method for pristine s-CNT network-based field effect transistors without surfactants or CNT bundles. First, Surfactant-dispersed s-CNT solution (purchased from NanoIntegris Inc., 99%) was diluted to ~1 μg/mL in DI water. A mixed cellulose ester membrane was settled on a vacuum filtration apparatus. The input pipe of the filtration apparatus was filled with the s-CNT solution, and the solution was filtered by applying vacuum on the opposite side of the membrane for 10 min. In this process, the s-CNTs were accumulated on the membrane. Subsequently, the membrane with attached s-CNT film was rinsed by DI water filtration for 10 min. In this process, the surfactants were rinsed by DI water and passed through the membrane. Then, the membrane was placed in a 2-propanol bath for 10 min to remove the residue of surfactants on the s-CNTs [29]. The rinsed membrane with the attached s-CNT film was placed in an acetone bath for 1 h. In this process, the membrane was dissolved by acetone to separate the s-CNT film from the membrane. The s-CNT film was picked up and placed into another acetone bath. We repeated the membrane dissolving process by 3 times to ensure the complete removal of the membrane. Then, the s-CNT film was placed into a methanol bath for 1 h. The s-CNT film was picked up and dried in air. Then, the surfactant-free s-CNT film was dispersed in 1,2-

dichlorobenzene (0.025 mg/mL) by a sonication for 5 h. A surfactant-free s-CNT solution was subjected to ultracentrifugation (Hitachi CS120GXL Micro Ultracentrifuge, Japan) at 400 000 RCF for 30 min in a vacuum. Here, Teflon based-centrifuge tubes were used to prevent the dissolution by 1,2-dichlorobenzene. After the centrifugation, the upper 30% portion of the s-CNT solution was extracted for device fabrication. To fabricate the pristine s-CNT network-based FETs, we utilized a "surface-programmed assembly" method. In this method, a SiO_2 substrate with octadecyltrichlorosilane (OTS) patterns was placed in the s-CNT solution for ~12 h so that s-CNTs in the solution were selectively assembled only on bare SiO_2 regions of the substrate. Lastly, the metal electrodes of Pd/Au (10 nm/15 nm) were patterned with photolithography followed by a thermal evaporation method.

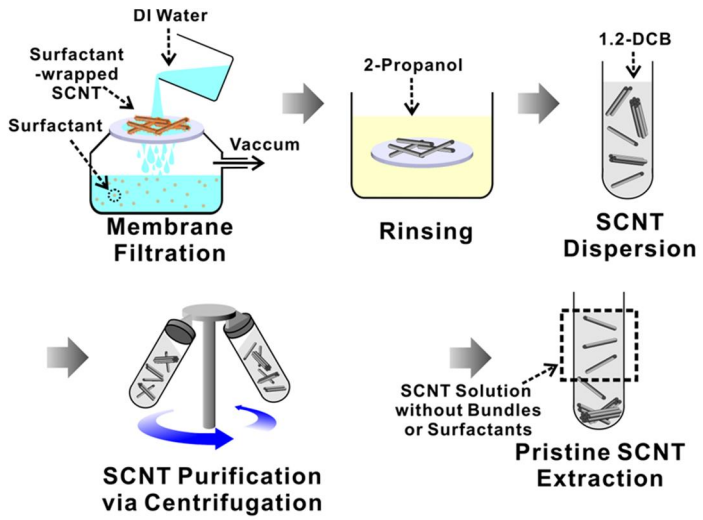

Fig. 2. 3 Preparation process of a pristine s-CNT solution

2.4.2 Fabrication of Pristine s-CNT-FET

Our pristine s-CNT network-based FETs were fabricated following the "surface programmed assembly" method as reported previously [30]. First, a photoresist (PR, Clariant Inc., AZ5214-E) was patterned on a SiO_2 substrate (oxide 1000 Å, Silicon Materials Inc.) via a photolithography. Subsequently, the PR patterned SiO_2 substrate was placed into octadecyltrichlorosilane solution (OTS, 1:500 v/v in hexane) for 6 min at 40% humidity and 23 °C. As a result, an OTS monolayer was formed on bare SiO_2 regions. The PR patterns on the substrate were dissolved by acetone. Then, the substrate was dipped into a pristine s-CNT solution for ~12 h. In this process, the pristine s-CNTs were selectively adsorbed onto bare SiO_2 regions without OTS monolayer patterns. Subsequently, the substrate was rinsed by 1,2-dichlorobenzene and dried by N_2 gas. Lastly, metal electrodes (15 nm thick Au on 10 nm thick Pd) were fabricated by photolithography, thermal evaporation, and lift-off processes.

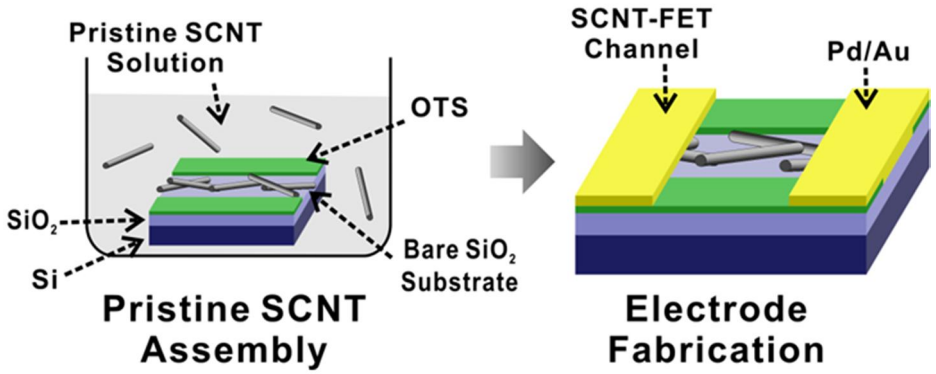

Fig. 2. 4 Fabrication of Pristine s-CNT-FET

2.5 Result and Discussion

2.5.1 Component Analysis of Pristine s-CNT Solution

After the centrifugation process, the concentration of s-CNT solutions may be uncertain, since we extracted the clean portion of the centrifuged s-CNT solutions. To estimate the actual concentration of s-CNT solutions after centrifugation processes, we utilized a spectrophotometric method (Fig. 2. 5 (a), (b)). At first, we measured the absorbance spectra of s-CNT solutions with known concentrations (0.003−0.1 mg/mL) using a UV−vis spectrophotometer (Agilent 8453) before the centrifugation process. The absorption spectra showed two peaks at 400−600 and 900− 1100 nm regions (Fig. 2. 5 (a)). The peak positions of the spectra were consistent with those of the third- and second-order van Hove transitions of semiconducting CNTs with its diameter of 1.2−1.7 nm [7, 31]. For detailed analysis, the optical absorbance of the s-CNT solutions at 465 nm was plotted as a function of s-CNT concentration values as shown in Fig. 2. 5 (b). Note that the absorbance values of s-CNT solutions were linearly proportional to the concentrations of the s-CNT solution. This indicates that we can estimate the concentration of s-CNT solutions from the optical absorbance plot. From the fitting curve in Fig. 2. 5 (b), the

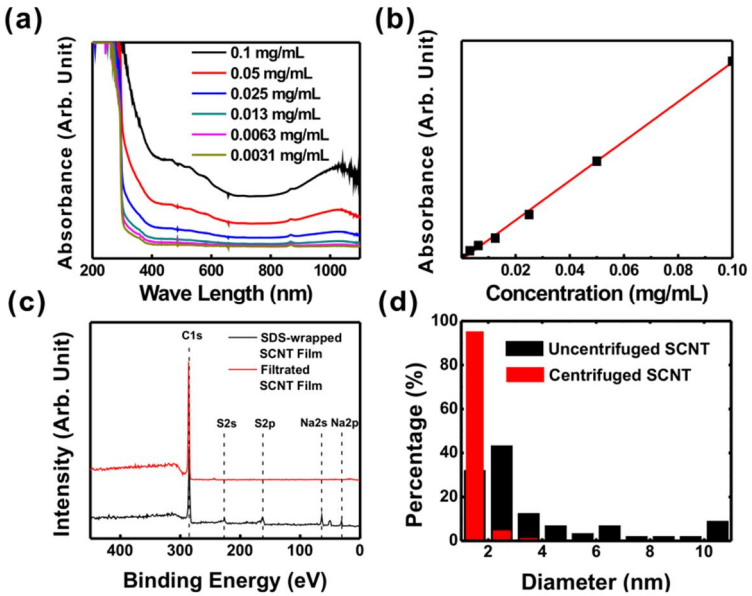

Fig. 2. 5 Component analysis of pristine s-CNT solution. (a) Optical absorbance of filtered s-CNT solutions with different concentrations. (b) Optical absorbance at 465 nm for s-CNT solutions with different concentrations. (c) XPS spectra of surfactant-wrapped s-CNT-based and filtered s-CNT-based films. (d) Diameter distribution of s-CNTs before and after the centrifugation process.

concentration of our centrifuged s-CNT solution was estimated as ~2 μg/mL.

To confirm that we prepared the solution of pristine s-CNTs without surfactant residues, we performed X-ray photoelectron spectroscopy (XPS) analysis. Fig. 2. 5 (c) shows the XPS spectra of surfactant-wrapped s-CNT-based and our pristine s-CNT-based films. Each film was prepared by a typical drop-cast method on a SiO_2 substrate [32]. The surfactant wrapped s-CNT-based film showed peaks at C 1s, S 2s, S2p, Na 2s, Na 2p, and I 4d positions. The peaks of S 2s, S 2p, Na 2s, and Na 2p could be associated with

residual surfactants as reported previously [33], and the small peak of I 4d could be associated with iodixanols which was used as a density gradient medium for the DGU process [7]. On the other hand, our pristine s-CNT-based film exhibited only a carbon peak of C 1s without any indication of residual surfactant molecules. This result clearly shows that the surfactant molecules on s-CNTs were successfully removed via our filtration method.

Fig. 2. 5 (d) shows the diameter distribution of s-CNTs before and after the centrifugation process. Here, s-CNTs were coated on a bare SiO_2 substrate, and the diameters of the s-CNTs were measured from AFM topography images. Note that more than 50% of uncentrifuged s-CNTs showed diameters larger than 2 nm, indicating a large amount of bundles (black histogram). However, about 95% of centrifuged s-CNTs showed diameters smaller than 2 nm (red histogram). This result clearly shows that we have successfully extracted the pristine s-CNTs without bundles using our purification method.

2.5.2 AFM and optical images of pristine s-CNT-based FETs

Fig. 2. 6 (a) and (b) show the AFM topography image of FET channels based on uncentrifuged and pristine s-CNTs, respectively. Here, we utilized the

surface programmed assembly process where OTS molecular patterns on SiO_2 substrates were utilized to selectively assemble s-CNTs from s-CNT solution onto the specific regions of the substrate [30]. Note that s-CNTs were selectively adsorbed onto bare SiO_2 regions (dark region), while an OTS molecular layer (white region) prevented the s-CNT adsorption. Fig. 2. 6 (a) shows that there existed a lot of CNT bundles in the FET channel based on uncentrifuged s-CNTs. From the height profile, the diameters of the uncentrifuged s-CNT bundles were estimated larger than 10 nm. Previous works showed that such CNT bundles could severely degrade the electrical performances of CNT network-based devices [31]. On the other hand, the FET channels based on centrifuged s-CNTs did not have many bundles (Fig. 2. 6 (b)). The height profile shows that the diameters of most of s-CNTs were 1−2 nm, indicating individual s-CNTs without bundles. The results clearly show that our method allowed us to prepare the patterns of s-CNT networks without bundles. It also should be noted that since our method relied only on conventional microfabrication facilities, we could apply our method for the wafer-scale fabrication of pristine s-CNT network-based devices (Fig. 2. 6 (c)).

Fig. 2. 6 (d) shows the effective thickness distribution of pristine s-CNT networks. The effective thickness was estimated from AFM

topographic images by dividing the pristine s-CNT network volume by the area of the patterned region [34]. Note that the effective thickness exhibited a sharp log-normal distribution, indicating a uniform percolated network of s-CNTs [30]. The averaged value of effective thickness was about 0.263 nm, which was much thinner than previous works using unpurified s-CNTs [34].

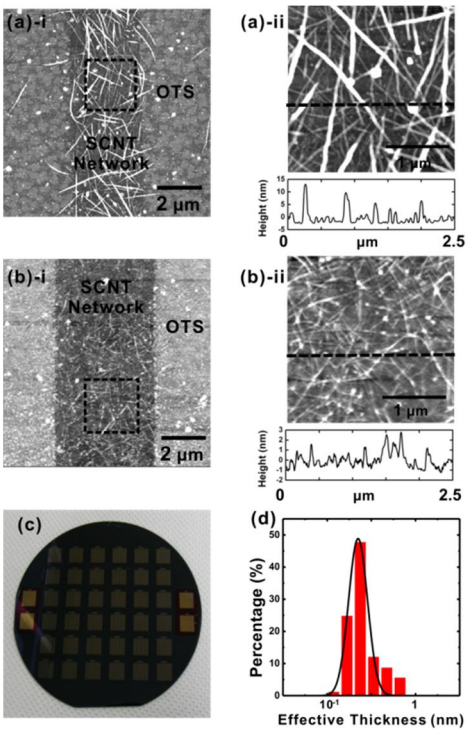

Fig. 2. 6 AFM and optical images of pristine s-CNT-based FETs. (a)-i: AFM topography image of an uncentrifuged s-CNT-based FET channel. There existed a lot of CNT bundles in the FET channel. (a)-ii: Magnified topography image of part (a)-i. The diameters of CNT bundles were often larger than 10 nm. (b)-i: AFM topography image of a pristine s-CNT-based FET channel. (b)-ii: Magnified topography image of part (b)-i. The diameters of most of s-CNTs were 1−2 nm. (c) Optical image of a large scale array of pristine s-CNT-based FETs fabricated on a Si/SiO2 wafer. (d) Effective thickness distribution of a pristine s-CNT network film. It can be fitted by a sharp log-normal distribution, indicating a percolated s-CNT network film.

2.5.3 Electrical characteristics of pristine s-CNT network-based FETs

Fig. 2. 7 (a) shows a schematic diagram depicting the structure of our pristine s-CNT network-based FET. In our FETs, multiple parallel CNT line patterns were utilized as a channel because such structures were reported to align s-CNTs and enable an improved device performance [34]. The width of individual line patterns was 2 μm, and the gap between individual channels was 4 μm. Each device had 10 separate channels of s-CNT networks. The channel length was 2 μm, unless specified otherwise.

The typical I−V characteristics of the pristine s-CNT network-based FET are shown in Fig. 2. 7 (b). The I−V characteristics of pristine s-CNT-FETs were measured by a semiconductor characterization system (Keithley, 4200-SCS). The bottom-gate bias was applied through a 100 nm thick SiO_2 layer. A source-drain bias was varied from 0.1 to 0.9 V, and a gate bias was swept from −20 to 20 V. The I−V curves with their gate bias range of −4 to 20 V clearly show a typical p-type behavior of CNTs, and the on−off ratio was $\sim 10^6$. However, the on-state current was saturated when the gate bias was smaller than −5 V, which has not been observed in previous s-CNT network-based devices [8-13]. This current saturation behavior could be explained by a simple model as shown in Fig. 2. 7 (c). First, when a s-CNT

is connecting between another s-CNT and a metal electrode, its resistance $R_{M\text{-}CNT}(V_G)$ can be written as

$$R_{M-CNT}(V_G) = r_{m-cnt}(V_G) + r_{cnt}(V_G) + r_{\mathrm{cnt-cnt}}$$
$$= r_{sb}(V_G) + r_i + r_{cnt}(V_G) + r_{\mathrm{cnt-cnt}}$$

where the $r_{m\text{-}cnt}$, r_{cnt} and $r_{cnt\text{-}cnt}$ represent the contact resistance of metal−CNT junctions, the resistance of s-CNTs, and the contact resistance of CNT−CNT junction, respectively. It should be also noted that the $r_{m\text{-}cnt}$ can be divided into two different terms: r_{sb}, a resistance associated with Schottky barriers between the s-CNT and the metal electrode, and r_i, a resistance associated with impurities or defects at the contact region. The r_{sb} should be strongly dependent on gate bias voltages, while r_i is not expected to vary much by the gate bias changes [35, 36] at a negative gate bias larger than the threshold voltage V_{th} of the s-CNT, the s-CNT channel will be turned on, and the r_{sb} and r_{cnt} become much smaller than r_i and $r_{cnt\text{-}cnt}$. Then, the total resistance $R_{M\text{-}CNT}$ can be approximated as a constant resistance like $R_{M\text{-}CNT} \cong r_i + r_{cnt\text{-}cnt}$. On the other hand, when a s-CNT is connecting between two CNTs of CNT1 and CNT2, its resistance $R_{CNT\text{-}CNT}(V_G)$ can be written as

$$R_{CNT-CNT}(V_G) = r_{cnt-cnt1} + r_{cnt}(V_G) + r_{\mathrm{cnt-cnt2}}$$

where the $r_{cnt\text{-}cnt1}$ and $r_{cnt\text{-}cnt2}$ represent the resistance at the contact with CNT1 and CNT2, respectively. By the same way, the resistance $R_{CNT\text{-}CNT}$ is

expected to saturate to a constant value $R_{CNT\text{-}CNT} \cong r_{cnt\text{-}cnt1} + r_{cnt\text{-}cnt2}$ at a large negative bias voltage. In case of network-based devices, the total resistance of the s-CNT networks can be described as serial or parallel connections of multiple resistances like $R_{M\text{-}CNT}$ and $R_{CNT\text{-}CNT}$. If individual s-CNTs in the networks have an identical threshold bias V_{th}, all s-CNTs in the network will be turned on at a similar negative bias V_{th} and have a constant resistance value. Thus, we can expect the total resistance of the network will have a constant value over a negative gate bias larger than V_{th}, and thus, the drain-source current will saturate. However, if the network includes a large amount of bundles and organic impurities, the threshold bias of individual bundles in the network may vary significantly, and some bundles may not be turned on even at a large negative gate bias. In this case, the network will not exhibit any saturation of the drain-source currents. This analysis implies that the saturation of drain-source currents at a large negative gate bias, as a matter of a fact, can be the intrinsic characteristics of s-CNT network devices comprised of individual pristine s-CNTs with a similar threshold voltage. Thus, the saturation behavior in Fig. 2. 7 (b) indicates that all individual s-CNTs in our network device had a similar threshold voltage, and they were all turned on at a negative gate bias below −5 V, resulting in the saturated drain-source currents. On the other hand, in most of previous works, the s-

CNT networks may include various bundles with largely varying threshold voltages, and some of the bundles may not be turned on even at a large negative gate bias. Thus, such networks did not exhibit the saturation of drain-source currents.

The removal of bundles and impurities in our process also improved the subthreshold swing. Fig. 2. 7 (d) shows the distribution of subthreshold swing values of uncentrifuged s-CNT-FETs and our pristine s-CNT-FETs. The subthreshold swing values of the pristine s-CNT-FETs were ~10 times smaller than those of the uncentrifuged s-CNT-FETs. The minimum subthreshold swing value of the pristine s-CNT-FET was ~490 mV/dec, which was similar to that of single-CNT-based devices with a similar gate structure [2, 4-6]. The small subthreshold swing values of our s-CNT-FETs can be attributed to the similar threshold voltages of individual s-CNTs in the networks. This indicates that our pristine s-CNT-FETs are suitable for the applications of high-performance integrated devices.

Fig. 2. 7 (e) shows the noise characteristics of an uncentrifuged s-CNT-FET and our pristine s-CNT-FET. For the noise measurement, we utilized a fast Fourier-transform network analyzer (SR 770). The 2 V of bias voltage was applied to the uncentrifuged s-CNT-FET and our pristine s-

CNT-FET. Both s-CNT-FETs exhibited a typical *1/f* noise behavior [37].

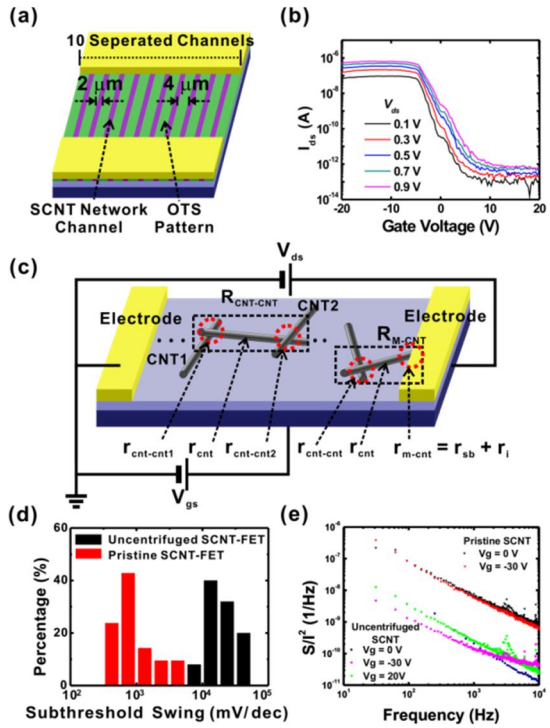

Fig. 2. 7 Electrical characteristics of pristine s-CNT network-based FETs. Electrical characteristics of pristine s-CNT network-based FETs. (a) Schematic diagram depicting the structure of our pristine s-CNT network based-FET. Purple and green regions represent s-CNT network channels and OTS monolayer-patterned regions, respectively. The device included 10 channels, and the width of individual channel was ~2 μm. The channel length of the devices in our works was ~2 μm unless specified otherwise. Pd/Au (10 nm/15 nm) electrodes were used as contacts. (b) I–V characteristics of a pristine s-CNT network-based FET with its channel length of ~2 μm. The device showed a p-type behavior. The on–off ratio was ~10^6. (c) Structure of pristine s-CNT network-based FETs. Note that the channel resistance is a linear combination of a CNT–metal electrode contact resistance r_{m-cnt}, a CNT resistance r_{cnt}, and a CNT–CNT contact resistance $r_{cnt-cnt}$. And the CNT–metal electrode contact resistance r_{m-cnt} can be divided into a gate voltage-dependent resistance r_{sb} originated from Schottky barriers and a constant resistance r_i originated from impurities and defects. (d) Distribution of subthreshold swing values of pristine s-CNT-FETs and uncentrifuged s-CNT-FETs. The subthreshold swing could be as small as ~490 mV/dec. (e) Noise characteristics of uncentrifuged s-CNT-FET and our pristine s-CNT-FET.

Note that the noise spectra of the uncentrifuged s-CNT-FET varied more unstably by the gate bias voltage changes than those of our pristine s-CNT-FET. Presumably, bundles and organic impurities in the uncentrifuged s-CNT networks lowered the stability of channel structures and worked as unstable noise sources. This result clearly shows that our process also can improve the stability of device channels in terms of its noise characteristics.

2.5.4 Scaling Behavior of s-CNT Network-based FETs.

Since our method allowed us to mass-produce devices based on pristine s-CNT networks, we could perform the statistical analysis and the scaling behavior study of multiple devices. Fig. 2. 8 (a) shows the on−off ratio distribution of uncentrifuged s-CNT-FETs and our pristine s-CNT-FETs with the structure shown in Fig. 2. 7 (a). The on−off ratios of the uncentrifuged s-CNT-FETs were smaller than $\sim 10^2$, while those of the pristine s-CNT-FETs were larger than 10^3 and more than 15% of the pristine s-CNT-FETs exhibited the on−off ratios larger than 10^6. Note that the on−off ratios of our devices were much larger than those of previous devices with similar structures [38]. It clearly shows that the removal of bundles and organic impurities can significantly improve the device performance. For example, although the portion of metallic CNTs in the uncentrifuged s-CNT

solution is small, any bundles including metallic CNTs would work as a metallic current path. Thus, metallic CNTs, if forming bundles, should generate more metallic current paths. Because of such metallic current paths, the uncentrifuged s-CNT-based FETs exhibited a rather high off-state conductance which reduced the on−off ratio [16]. Furthermore, the organic impurities might increase the contact resistance and reduce the saturation currents of the devices and thus the on−off ratio.

Fig. 2. 8 (b) shows the on−off ratio distribution of our pristine s-CNT-FETs with different channel lengths. Note that the devices with the channel lengths of 2−10 μm exhibited a similar distribution of on−off ratios. Previous works showed that when a number of metallic CNTs formed a percolated network in the network-based devices, the increased channel length reduced the formation of percolated networks of metallic current paths and, thus, improved the on−off ratios of the devices [8, 10 , 11, 39]. However, our pristine s-CNT-FETs exhibited a similar on−off ratio distribution in these channel length ranges, implying that the metallic paths in our devices were minimal. In this case, the on−off ratios should be mainly determined by the saturated on-currents as shown in Fig. 2. 7 (b). Here, when s-CNTs in network-based devices were turned on at a large negative bias voltage, contact resistances in the network remained and limited on-currents, which, in effect, limited the on−off ratio of our devices. Thus, in the case of pristine

s-CNT-FETs with a minimal metallic path, the saturated on-current, which was mainly determined by contact resistances, is one of the most important parameters determining the device performances. Also, we estimated the mobility of the devices using a classical mobility equation, $\mu = (dI_{ds}/dV_g)(L^2/C_g)(1/V_{ds})$, and a parallel plate capacitor model [34]. Here, L and C_g represent the channel length and the gate capacitance, respectively. The mobility of the devices with its channel length larger than 10 μm was ~140 $cm^2/(V \cdot s)$, which is similar to or better than the values reported in previous works [38]. The devices with a rather short channel length (L = 2 μm) exhibited a bit low mobility of ~24 $cm^2/(V \cdot s)$, which could be attributed to the increased portion of contact resistance between CNTs and metal electrodes to the entire current paths of the devices.

Fig. 2. 8 (c) shows the on-state conductance distribution of pristine s-CNT-FETs with its channel length of 2 μm. It showed a log-normal distribution, which indicates that our device channels, when it was turned on, can be described as a percolated network of resistances [30, 40]. Presumably, at a large negative gate bias, all s-CNTs were turned on, and only contact resistance components r_i and $r_{cnt\text{-}cnt}$ remained to form a percolated resistance networks.

Fig. 2. 8 (d) shows the averaged on-state resistance of pristine s-

CNT-FETs with rather long channel lengths. In the case of long channels, the resistance was linearly proportional to the device channel length, indicating that the resistance of pristine s-CNT networks increased linearly with an increased channel length. From the slope of the linear fitting curve and the shape of our channels, we can estimate the sheet resistance of our pristine s-CNT networks. Note that when the device was turned on, the s-CNT network could be modeled as a network of contact resistances $r_{cnt\text{-}cnt}$ between s-CNTs. Here, the numbers of CNT−CNT contacts were first estimated using an AFM topography image of s-CNT networks. The averaged number of the CNT−CNT contacts was about 41.1 per μm^2. Then, from the sheet resistance and the number of CNT−CNT contacts, the contact resistance $r_{cnt\text{-}cnt}$ between individual CNTs could be estimated as 213 kΩ, which is similar to previously estimated values [40]. It is also interesting to note that the fitting curve intercepted the y-axis at a nonzero value, which should represent total contact resistance between metal electrodes and s-CNT networks. Here, we estimated the averaged number of contacts between a metal electrode and individual s-CNTs. Then, from the y-intercept value and the number of contacts, we could estimate the contact resistance r_i between our palladium electrode and individual s-CNTs as ~11.7 MΩ. This result is also consistent with previously reported results [41]. These results confirm that the electrical

characteristics of a pristine s-CNT-FET can be described by our model based on resistance networks as shown in Fig. 2. 7 (c).

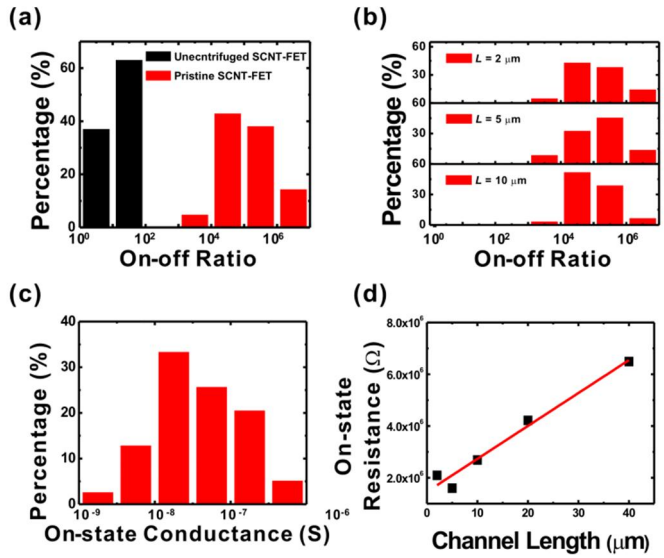

Fig. 2. 8 Scaling behavior of s-CNT network-based FETs. (a) On−off ratio distribution of uncentrifuged s-CNT-FETs and our pristine s-CNT-FETs. (b) On−off ratio distribution of our pristine s-CNT-FETs with different channel lengths. The on−off ratio did not change much with different channel lengths. (c) On-state conductance distribution of our pristine CNT-FETs. The distribution shows a log-normal distribution. (d) Averaged on-state resistance of pristine s-CNT-FETs with different channel lengths. The resistance of the device with a rather long channel length was found to be linearly proportional to the channel length. The solid line represents a linear fitting curve. The slope and intercept are 127 kΩ/μm and 1.46 MΩ, respectively.

2.5 Summary

In summary, we developed a method for the large scale assembly of pristine s-CNT network-based devices without bundles or organic impurities, thus exhibiting its intrinsic characteristics. The device exhibited an improved on−off ratio up to over $\sim 10^6$ and a subthreshold swing value down to $\sim$

490 mV/dec. Interestingly, our pristine s-CNT network-based FET exhibited a saturated drain-source current at a large negative gate bias. Such improved performance and anomalous saturation behavior were attributed to the uniform threshold voltage of the current paths in our pristine s-CNT networks. Furthermore, the scaling behavior analysis indicates that the performance of FETs based on pristine s-CNT networks without metallic paths can be limited by the contact resistance components which are independent of gate bias voltages. Since our works reveal valuable insights about the intrinsic characteristics and fundamental limitations of pristine s-CNT network devices without metallic paths, it can be an important stepping stone toward the high-performance s-CNT device applications in the future.

References

[1] B. Q. Wei, R. Vajtai, P. M. Ajayan, Reliability and current carrying capacity of carbon nanotubes. *Appl. Phys. Lett.* **79**, 1172-1174 (2001).

[2] R. V. Seidel et al., Sub-20 nm short channel carbon nanotube transistors. *Nano Lett.* **5**, 147-150 (2005).

[3] X. J. Zhou, J. Y. Park, S. M. Huang, J. Liu, P. L. McEuen, Band structure, phonon scattering, and the performance limit of single-walled carbon nanotube transistors. *Phys. Rev. Lett.* **95**, 146805 (2005).

[4] A. Javey et al., High-kappa dielectrics for advanced carbon-nanotube transistors and logic gates. *Nat. Mater.* **1**, 241-246 (2002).

[5] Z. X. Wang et al., Growth and Performance of Yttrium Oxide as an Ideal High-kappa Gate Dielectric for Carbon-Based Electronics. *Nano. Lett.* **10**, 2024-2030 (2010).

[6] J. Appenzeller et al., Field-modulated carrier transport in carbon nanotube transistors. *Phys. Rev. Lett.* **89**, 126801 (2002).

[7] M. S. Arnold, A. A. Green, J. F. Hulvat, S. I. Stupp, M. C. Hersam, Sorting carbon nanotubes by electronic structure using density differentiation. *Nat. Nanotechnol.* **1**, 60-65 (2006).

[8] B. Chandra, H. Park, A. Maarouf, G. J. Martyna, G. S. Tulevski, Carbon nanotube thin film transistors on flexible substrates. *Appl. Phys. Lett.* **99**, 072110 (2011).

[9] A. A. Green, M. C. Hersam, Nearly Single-Chirality Single-Walled Carbon Nanotubes Produced via Orthogonal Iterative Density Gradient Ultracentrifugation. *Adv. Mater.* **23**, 2185-2190 (2011).

[10] C. Wang et al., Extremely Bendable, High-Performance Integrated Circuits Using Semiconducting Carbon Nanotube Networks for Digital, Analog, and Radio-Frequency Applications. *Nano Lett.* **12**, 1527-1533 (2012).

[11] C. A. Wang, J. L. Zhang, C. W. Zhou, Macroelectronic Integrated Circuits Using High-Performance Separated Carbon Nanotube Thin-Film Transistors. *Acs Nano* **4**, 7123-7132 (2010).

[12] A. A. Green, M. C. Hersam, Properties and Application of Double-Walled Carbon Nanotubes Sorted by Outer-Wall Electronic Type. *Acs Nano* **5**, 1459-1467 (2011).

[13] V. K. Sangwan et al., Fundamental Performance Limits of Carbon Nanotube Thin-Film

Transistors Achieved Using Hybrid Molecular Dielectrics. *Acs Nano* **6**, 7480-7488 (2012).

[14] K. Ryu et al., CMOS-Analogous Wafer-Scale Nanotube-on-Insulator Approach for Submicrometer Devices and Integrated Circuits Using Aligned Nanotubes. *Nano Lett.* **9**, 189-197 (2009).

[15] N. Rouhi, D. Jain, K. Zand, P. J. Burke, Fundamental Limits on the Mobility of Nanotube-Based Semiconducting Inks. *Adv. Mater.* **23**, 94-99 (2011).

[16] C. W. Lee et al., Toward high-performance solution-processed carbon nanotube network transistors by removing nanotube bundles. *J. Phys. Chem. C* **112**, 12089-12091 (2008).

[17] V. Derycke, R. Martel, J. Appenzeller, P. Avouris, Controlling doping and carrier injection in carbon nanotube transistors. *Appl. Phys. Lett.* **80**, 2773-2775 (2002).

[18] Z. W. Pan, Z. R. Dai, Z. L. Wang, Nanobelts of semiconducting oxides. *Science* **291**, 1947-1949 (2001).

[19] S. Myung, M. Lee, G. T. Kim, J. S. Ha, S. Hong, Large-scale "surface-programmed assembly" of pristine vanadium oxide nanowire-based devices. *Adv. Mater.* **17**, 2361-2364 (2005).

[20] S. H. Hong, C. A. Mirkin, A nanoplotter with both parallel and serial writing capabilities. *Science* **288**, 1808-1811 (2000).

[21] S. H. Hong, J. Zhu, C. A. Mirkin, Multiple ink nanolithography: Toward a multiple-pen nano-plotter. *Science* **286**, 523-525 (1999).

[22] R. D. Piner, J. Zhu, F. Xu, S. H. Hong, C. A. Mirkin, "Dip-pen" nanolithography. *Science* **283**, 661-663 (1999).

[23] Y. Li, B. W. Maynor, J. Liu, Electrochemical AFM "dip-pen" nanolithography. *J. Am. Chem. Soc.* **123**, 2105-2106 (2001).

[24] A. Ivanisevic, C. A. Mirkin, "Dip-Pen" nanolithography on semiconductor surfaces. *J. Am. Chem. Soc.* **123**, 7887-7889 (2001).

[25] A. Kumar, G. M. Whitesides, Features of Gold Having Micrometer to Centimeter Dimensions Can Be Formed through a Combination of Stamping with an Elastomeric Stamp and an Alkanethiol Ink Followed by Chemical Etching. *Appl. Phys. Lett.* **63**, 2002-2004 (1993).

[26] Y. N. Xia, G. M. Whitesides, Soft lithography. *Angew. Chem. Int. Edit.* **37**, 550-575 (1998).

[27] Y. N. Xia, J. A. Rogers, K. E. Paul, G. M. Whitesides, Unconventional methods for fabricating and patterning nanostructures. *Chem. Rev.* **99**, 1823-1848 (1999).

[28] R.C. Jaeger, Introduction to Microelectronic Fabrication. *Prentice Hall, New Jersey,* vol **V**, 2nd ed, Chap. 2, 2002.

[29] Z. C. Wu et al., Transparent, conductive carbon nanotube films. *Science* **305**, 1273-1276 (2004).

[30] M. Lee et al., Linker-free directed assembly of high-performance integrated devices based on nanotubes and nanowires. *Nat. Nanotechnol.* **1**, 66-71 (2006).

[31] R. B. Weisman, S. M. Bachilo, Dependence of optical transition energies on structure for single-walled carbon nanotubes in aqueous suspension: An empirical Kataura plot. *Nano Lett.* **3**, 1235-1238 (2003).

[32] N. Minami, Y. J. Kim, K. Miyashita, S. Kazaoui, B. Nalini, Cellulose derivatives as excellent dispersants for single-wall carbon nanotubes as demonstrated by absorption and photoluminescence spectroscopy. *Appl. Phys. Lett.* **88**, 093123 (2006).

[33] H. Z. Geng et al., Effect of acid treatment on carbon nanotube-based flexible transparent conducting films. *J. Am. Chem. Soc.* **129**, 7758-7759 (2007).

[34] M. Lee et al., "Textured" Network Devices: Overcoming Fundamental Limitations Limitations of Nanotube/Nanowire Network-Based Devices. *Small* **5**, 1642-1648 (2009).

[35] J. Tersoff, Contact resistance of carbon nanotubes. *Appl. Phys. Lett.* **74**, 2122-2124 (1999).

[36] M. S. Fuhrer et al., Crossed nanotube junctions. *Science* **288**, 494-497 (2000).

[37] S. Soliveres, J. Gyani, C. Delseny, A. Hoffmann, F. Pascal, 1/f noise and percolation in carbon nanotube random networks. Appl. Phys. Lett. **90**, 082107 (2007).

[38] J. Lee et al., Floating electrode transistor based on purified semiconducting carbon nanotubes for high source-drain voltage operation. *Nanotechnology* **23**, 085204 (2012).

[39] C. Wang et al., Wafer-Scale Fabrication of Separated Carbon Nanotube Thin-Film Transistors for Display Applications. *Nano Lett.* **9**, 4285-4291 (2009).

[40] M. Lee et al., 100 nm scale low-noise sensors based on aligned carbon nanotube networks: overcoming the fundamental limitation of network-based sensors. *Nanotechnology* **21**, 055504 (2010).

[41] Y. Woo, G. S. Duesberg, S. Roth, Reduced contact resistance between an individual single-walled carbon nanotube and a metal electrode by a local point annealing. *Nanotechnology* **18**, 095203 (2007).

Chapter 3.
Scanning Noise Microscopy on Sorted CNT Network

3.1 Introduction

Nano materials based electronic devices have been extensively studied due to their possibility for future electronics. One key parameter for determining the characteristics of a nano material is a current noise [1, 2]. The noise of a nano device is determined by various material properties such as defects in lattices [3, 4], an energy barrier [5, 6], a carrier number [7] and a mobility [8]. Therefore, analyzing a noise can provide a great deal of information about a nano device. However, current measurement techniques for analyzing noises still rely on old technologies. Using the previous techniques, researchers could only measure the total amount of noises that occur when a current passing through the channel of a device [9-14]. Thus, researchers couldn't identify where the noise of a device occurs, though the statistical noise characteristics of a device could be measured. To solve this problem, recently, a "noise spectral imaging (NSI)" method was developed [15]. This method allowed us to measure the noise source density maps of graphene domains via a modified conducting atonic force microscopy (AFM)

technique. The NSI method has several advantages. First, it is possible to map the noise sources distributed in device channels. Second, the NSI method is a non-destructive test. Third, during noise imaging, contact-mode AFM measurements such as current imaging can be performed simultaneously. Especially, the last advantage allows more complex analysis of noises in nano materials. However, the NSI technique has not been employed for the noise measurements of carbon nanotube (CNT) networks.

Carbon nanotube is one of promising material for future electronics due to its excellent electrical characteristics such as a high conductivity, a high carrier density, a high mobility, a high on-off ratio and a low subthreshold swing. Despite the excellent electrical characteristics, electrical device applications using CNTs are limited by a high current noise at a low-frequency region. Many researchers studied about the noise of CNTs to understand the main reason of the noise. As a result, many researchers showed that the main reason of noise of CNT devices is a carrier number fluctuation caused by charge traps in oxide layers and channels [12-14]. However, previous researches couldn't enable the mapping of localized noise sources in a CNT channel.

Herein, we report a method for the direct imaging of electrical noise sources and mobilities in carbon nanotube networks. In this study, we measured the current maps and the electrical noise power spectral density

(PSD) maps of semiconducting and metallic CNT networks via a modified conducting AFM system. Then, the PSD maps and the current maps were analyzed via a finite elemental method (FEM) analysis and a differential method, enabling the mapping of the distribution of localized electrical noise sources and mobilities in the CNT networks. In the case of a metallic CNT network, we found that the noise activities were just depending on the diameter of each CNT and the density of CNT network. Also, in the case of a semiconducting CNT network, we found that the noise activities were high at crossed-CNT junctions. Also, we calculated the mobility map of a semiconducting CNT network via a FEM method. To clearly show the difference of noise characteristics between semiconducting and metallic CNTs, we performed a NSI method on a cross-patterned CNT network. Here, we made cross-patterns on SiO2 substrate by adsorbing semiconducting CNT networks and metallic CNT networks orthogonally. Our experiment should allow understanding the noise behavior of metallic and semiconducting CNTs, and should have a significant impact on CNT-based electronics.

3.2 Low-Frequency Noise

Electrical noise can severely degrade the performance of electronic

devices. Particularly, the low frequency noise can be a critical problem hindering the practical applications of those electronic devices1. It was previously reported that 1/*f* noise is a significant problem in the devices based on semiconducting nanomaterials such as carbon nanotubes [12-14, 16-19], graphene [20-23], and nanowires (NWs) [24, 25]. Thus, the 1/*f* noise has been extensively studied by many researchers. To explain the origins of 1/*f* noise in semiconducting materials, several different theories have been established previously. One of the theories is the carrier number fluctuation theory [26-29], which was firstly proposed by McWhorter [26]. In that theory, the physical origin of 1/*f* noise generated in typical Si-based devices was explained by a simple mathematical model. Briefly, the 1/*f* noise of Si-based devices is mainly attributed to the random trapping and detrapping processes of charge carriers in the charge traps at the Si/SiO_2 interface. Here, individual noise sources can trap and release charge carriers with a relaxation time τ. The repeated trapping and detrapping of the charge carriers result in the current fluctuations whose power spectral density (PSD) is proportional to $\sim 1/f^2$. If the current channel has a large number of noise sources with different relaxation time τ, the noise PSD of the different noise sources are overlapped and result in the noise spectra proportional to 1/*f*. Here, the 1/*f* noise can be represented by an empirical expression that describes the

current PSD, given by [1, 30, 31].

$$S_I = A\frac{I^2}{f^\alpha}$$

where the exponent α (~1.0) is a scaling factor of frequency. The *I* and *A* represent the current and the noise amplitude, respectively. Note that the noise amplitude *A* show the fundamental noise characteristics of the devices.

3.3 1/*f* Noises in Nanomaterials

Note that as the dimension or the operating voltage of electronic devices were reduced, their low frequency noise increased and became a critical parameter determining the electrical performance of the devices [32]. Therefore, low frequency noise in the devices based on various nanomaterials has been extensively studied by many researchers. For example, previous works show that CNT-based devices have a rather large 1/*f* noise compared to conventional semiconducting devices.

Fig. 3. 1 shows the previously-reported noise characteristics of CNT-based channels [16]. Note that the noise amplitude *A* for the devices based on a bulk CNT network channel was proportional to the resistance *R* of the CNT-based device like $A \sim 10^{-11} \times R$. In case of rectangular-shaped CNT network channels, the channel width and length were reported to

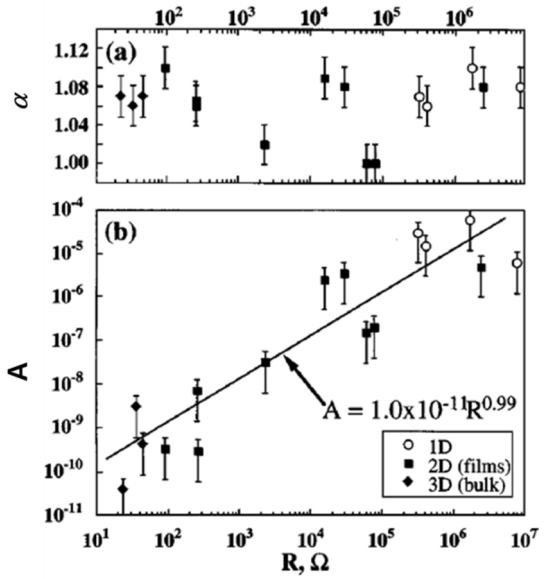

Fig. 3. 1 Noise characteristics of CNT-based channels (a) scaling parameters for a wide range of CNT-based channels as a function of sample resistance [16]. (b) Variation of noise amplitude *A* for the same sample set. A least-squares power law fit suggests a direct proportionality between noise amplitude *A* and sample resistance *R*

significantly affect the noise behaviors. Although, the FETs based on *aligned* CNT networks in the nano-scale-width channels exhibited improved electrical performances compared with those based on random CNT networks, their increased noise level was a major hurdle for practical applications, and we do not even have a model to describe the noise characteristics of such nano-scale-channel-width devices. In addition, graphene has recently attracted significant interest as a promising material for electronic applications because of its superb electrical transport characteristics such as high conductivity and mobility. However, graphene-

based devices have also shown the rather high 1/*f* noise which can hinder its nanoelectronic applications.

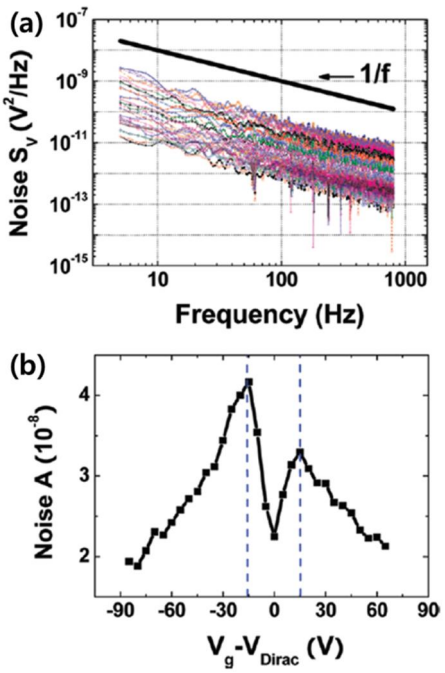

Fig. 3. 2 Noise characteristics of SLG [23]. (a) Voltage PSD of SLG samples with gate biases varying from -50 to 100 V (step =5 V). (b) Noise amplitude A versus gate bias V_g - V_{Dirac} for the SLG samples.

The typical noise characteristics of graphene-based devices were shown in Fig. 3. 2 Previous works showed that the noise of graphene-based devices strongly depends on a gate bias voltage, and this noise behavior could be explained by spatial charge inhomogeneity [23]. Interestingly, double-layer graphene exhibited much lower noise than single-layer graphene. However, it should be noted that these extraordinary noise behaviors of graphene were not fully understood yet.

3.4 Calculation of Conductivity Map on 2-D Materials

Fig. 3. 3 shows a schematic diagram depicting a 2-D material measured via our NSI system. A nanoscale conducting AFM probe made a direct contact on the surface of a 2-D material and scanned the region marked by the black solid line ("scanned region"). While scanning, a constant bias voltage was maintained between the probe and the electrode, and the electrical current and noise signals through the probe were measured to calculate the conductivity map and noise source distribution of the 2-D material.

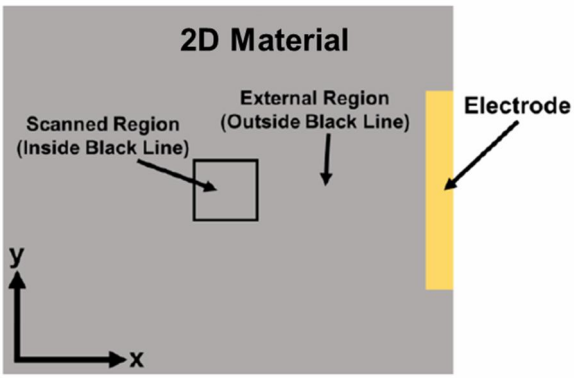

Fig. 3. 3 Schematic diagram showing a graphene sheet with an electrode. A nanoscale conducting AFM probe made a direct contact on a graphene sheet (marked by gray area) with a constant contact force, and it scanned inside the "scanned region" marked by a black solid line. During the scanning, a constant bias voltage was applied between the electrode and the probe, and the electrical noises and currents through the probe were measured at each point of the region.

We developed an iterative method to calculate the conductivity map of the 2-D material from the measured current. Note that the current maps exhibited clear contrasts with a nanoscale resolution, implying that the variations of current values in the maps were determined by the localized sheet resistance values of the nearby regions rather than those of far-away regions. Thus, in the case of Fig. 3.3, we can assume that the sheet resistance in the external region has a constant value, and the variation of sheet resistance values in the scanned region caused the variation of electrical currents through the probe. Then, the sheet resistance values of the external region and each point in the scanned region were calculated numerically using an iterative method as following.

As a first step, we calculated the sheet resistance value in the external region using an iterative method. Here, we assumed that the probe is placed at the center of the scanned region and the entire sheet has a uniform sheet resistance value reported in literatures [33]. Then, the algorithms coded in Agros2D (http://agros2d.org) were used to calculate the electrical currents ($I_{simulation}$) through the probe. Using the Agros2D algorithms, the scalar electric potential V (x, y) at each point of 2-D material was calculated by solving the quasi-harmonic equation as following [34].

$$\frac{\partial}{\partial x}\left(\frac{1}{R_S(x,y)}\cdot\frac{\partial V(x,y)}{\partial x}\right)+\frac{\partial}{\partial y}\left(\frac{1}{R_S(x,y)}\cdot\frac{\partial V(x,y)}{\partial y}\right)=0 \qquad \text{(Eq. 3. 1)}$$

where $R_s(x, y)$ represents the sheet resistance at (x, y). Here, the boundary condition of a fixed potential $V(x, y)$ was applied to the conducting probe and the electrode, respectively. Also, a Neumann boundary condition of zero was imposed to the outer edges of the 2-D material to prohibit currents flowing out of the 2-D material sheet. Then, the map of the electric field $E(x, y)$ on the graphene sheet was obtained by taking the gradient of the $V(x, y)$, and a current density $J(x, y)$ map could be obtained from the calculated E map using the relation

$$J(\mathrm{x}, \mathrm{y}) = \frac{1}{R_S(x,y)} E(x, y) \qquad \text{(Eq. 3. 2)}$$

Finally, the electrical currents $I_{simulation}$ through the probe could be calculated by integrating the current densities over the electrode surface. Then, we compared the $I_{simulation}$ with the averaged current value I_{avg} of the measured current map. If the $I_{simulation}$ was higher or lower than the I_{avg}, we recalculated $I_{simulation}$ assuming a larger or smaller R_{avg} value. We repeated the iteration using a secant algorithm [35] until we obtained a R_{avg} value to make the $I_{simulation}$ close to the I_{avg} with a less than 0.1% error.

The obtained R_{avg} was utilized as a sheet resistance value R_{ext} of the external region for the iterative calculation of the sheet resistance value at each point in the scanned region. Initially, we assumed a uniform sheet resistance $R_{scanned}(x, y) = R_{ext}$ in the scanned region, and the current $I_{simulation}$

(x, y) through the probe located at (x, y) was calculated using the same Agros2D algorithm. Then, $R_{scanned}(x, y)$ was adjusted following the secant algorithm until we obtained the sheet resistance value $R_{ini}(x, y)$ to make the $I_{simulation}(x, y)$ close to the current value $I_{measured}(x, y)$ in the measured current map with a less than 0.1% error. The calculation was repeated over all $l_{ocation}(x, y)$ in the scanned region to obtain the map of sheet resistance value $R_{ini}(x, y)$ of the 2-D material in the scanned region.

The obtained $R_{\underline{ini}}(x, y)$ was used as an initial sheet resistance value at (x, y) for further simulation to calculate more precise sheet resistance value R (x, y) of the 2-D material in the scanned region. Here, we first assumed the uniform sheet resistance R_{ext} in the external region and the initial sheet resistance $R_{ini}(x, y)$ in the scanned region, and the electrical currents through the probe located at (x, y) were calculated using the Agros2D algorithm. Then, the sheet resistance value $R(x, y)$ of the 2-D material at (x, y) was adjusted using a secant algorithm [35] until we obtained the sheet resistance value $R(x, y)$ to make the $I_{simulation}(x, y)$ close to the current value $I_{measured}(x, y)$ in the measured current map with a less than 10 % error. The calculation was repeated over all location (x, y) in the scanned region to obtain the map of sheet resistance value $R(x, y)$ of the 2-D material at (x, y) in the scanned region.

Using the obtained sheet resistance map $R(x, y)$, we performed the

repeated calculation to update $R(x, y)$ for more precise values. We repeated the calculation to continually update the sheet resistance value $R(x, y)$ of the 2-D material in the scanned region until the $I_{simulation}(x, y)$ over all points in the scanned region became close to the current value $I_{measured}(x, y)$ in the measured current map with a less than 10 % error. Finally, the obtained $R(x, y)$ was used to calculate the conductivity map of $\sigma(x, y)$ using the relation $\sigma(x, y) = 1/(t(x, y) \cdot R(x, y))$. Here, $t(x, y)$ is the thickness of a 2-D material at (x, y).

3.5 Calculation of a Noise Source Density Map on 2-D Materials

For the calculation of the noise source distribution from a noise PSD map, we modeled a 2-D material as a network of resistors with noise sources (Fig. 3. 4). At first, let us consider a node 0 at (x, y) position as shown in Fig. 3. 4. The node 0 is connected to four different nodes i (i = 1, 2, 3, and 4) through four small resistors whose resistances were ΔR_i. Each resistor generates the current noise ΔS_i. For square lattice, ΔR_i is the same as sheet resistance R_s of the 2-D material. Further, when Δl is small, the variation of ΔR_i for a specific node is much smaller than ΔR_i. Thus, we can approximate all of ΔR_i (i =1, 2, 3, and 4) as their averaged value of ~ ΔR, and the sheet

resistance map obtained using our computational method could be utilized to obtain a ΔR_i value at the node 0. The R_i (i =1, 2, 3, and 4) represents the effective resistance of the total current paths between the node i and the metal electrode excluding the current paths passing through the node 0. Note that the finite element method simulation used to estimate the sheet resistance map provided the current density map, enabling the estimation of the I_1, I_2, I_3, and I_4. Using the values, the R_i values could be obtained using the Ohm's law,

$$V = (R_i + \Delta R) \cdot I_i \qquad \text{(Eq. 3. 3)}$$

In our network model, all of the resistors were assumed as independent noise sources as shown in Fig. 3. 4. In general, when two independent noise sources i (i = 1, 2) are connected in parallel, the total current PSD is given by

$$S_{total} = S_{I1} + S_{I2} \qquad \text{(Eq. 3. 4)}$$

On the other hand, when two independent noise sources are connected in series, the total current PSD is given by

$$S_{total} = \frac{S_{V1} + S_{V2}}{(R_1 + R_2)^2} = \left(\frac{R_1}{R_1+R_2}\right)^2 S_{I1} + \left(\frac{R_2}{R_1+R_2}\right)^2 S_{I2} \qquad \text{(Eq. 3. 5)}$$

where R_i and S_{Ii} (i = 1, 2, 3, 4) correspond to the *resistance* and *generated current noise* of each resistor with noise sources, respectively.

The equations (Eq. 3. 4) and (Eq. 3. 5) imply that if we have local

resistance information, we can calculate the current PSD for individual noise sources in the network system. Therefore, we could obtain the current PSD ΔS_I from the resistance ΔR, using the sheet resistance map. Here, S_{Ii} and ΔS_{Ii} correspond to the current PSD generated by the resistors of R_i and ΔR_i, respectively. We can also approximate all of the ΔS_{Ii} as their averaged value ΔS.

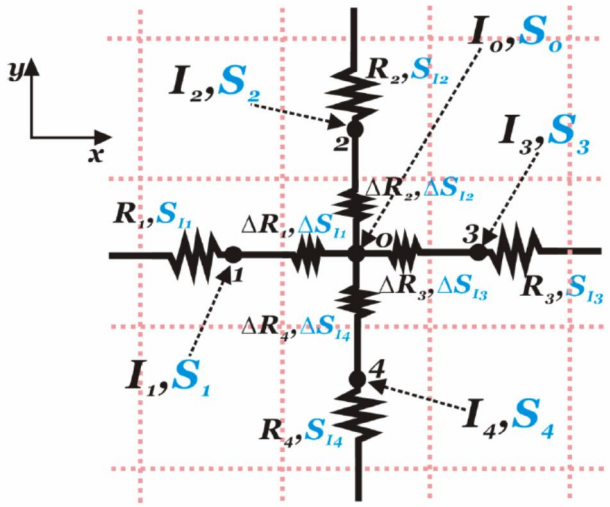

Fig. 3. 4 Circuit diagram of the resistance network representing a graphene sheet. The graphene sheet was assumed as a resistor network. In our network model, every single node (*node 0*) is connected to its neighbor nodes (*node 1, 2, 3, and 4*) by a small resistance ΔR.

Using the equation (Eq. 3. 4) and (Eq. 3. 5), the current PSD S_I measured at the node 1 (Fig. 3. 4) can be calculated like,

$$S_1 = \left(\frac{\left(\frac{1}{\frac{1}{r_1-\Delta R}+\frac{1}{r_2}+\frac{1}{r_3}+\frac{1}{r_4}}\right)}{\left(\frac{1}{\frac{1}{r_1-\Delta R}+\frac{1}{r_2}+\frac{1}{r_3}+\frac{1}{r_4}}\right)+R_c}\right)^2 \cdot \left(S_{I_1} + \left\{\left(\frac{\Delta R}{\Delta R+\frac{1}{\frac{1}{r_2}+\frac{1}{r_3}+\frac{1}{r_4}}}\right)^2 \cdot \Delta S + \left(\frac{\frac{1}{\frac{1}{r_2}+\frac{1}{r_3}+\frac{1}{r_4}}}{\Delta R+\frac{1}{\frac{1}{r_2}+\frac{1}{r_3}+\frac{1}{r_4}}}\right)^2 \cdot \left(S_{I_2+\Delta I} + S_{I_3+\Delta I} + S_{I_4+\Delta I}\right)\right\}\right) + \left(\frac{R_c}{\left(\frac{1}{\frac{1}{r_1-\Delta R}+\frac{1}{r_2}+\frac{1}{r_3}+\frac{1}{r_4}}\right)+R_c}\right)^2 \cdot S_{I_c} \quad \text{(Eq. 3. 6)}$$

The $S_{I_i+\Delta I}$, and S_{I_c} correspond to the current PSD from the resistance r_i (=R_i +ΔR) and the *contact resistance* R_c, respectively. Note that the $S_{I_i+\Delta I}$ in the equation (Eq 3. 6) can be written in terms of S_{I_i} and ΔS like,

$$S_{I_i+\Delta I} = \left(\frac{R_i}{R_i+\Delta R}\right)^2 S_{I_i} + \left(\frac{\Delta R}{R_i+\Delta R}\right)^2 \Delta S \quad \text{(Eq. 3. 7)}$$

Since the contact resistance R_c is much smaller than R_i or r_i, the equation (Eq. 3. 6) can be approximated as

$$S_1 \approx \left(S_{I_1} + \left\{\left(\frac{\Delta R}{\Delta R+\frac{1}{\frac{1}{r_2}+\frac{1}{r_3}+\frac{1}{r_4}}}\right)^2 \cdot \Delta S + \left(\frac{\frac{1}{\frac{1}{r_2}+\frac{1}{r_3}+\frac{1}{r_4}}}{\Delta R+\frac{1}{\frac{1}{r_2}+\frac{1}{r_3}+\frac{1}{r_4}}}\right)^2 \cdot \left(S_{I_2+\Delta I} + S_{I_3+\Delta I} + S_{I_4+\Delta I}\right)\right\}\right) \quad \text{(Eq. 3. 8)}$$

Given that the ΔR is much smaller than R_i or r_i, the equation (Eq. 3. 8) can be further approximated as

$$S_1 \approx S_{I_1} + \left(\Delta R\left(\frac{1}{r_2}+\frac{1}{r_3}+\frac{1}{r_4}\right)\right)^2 \cdot \Delta S + \left(\frac{1}{1+\Delta R\left(\frac{1}{r_2}+\frac{1}{r_3}+\frac{1}{r_4}\right)}\right)^2 \cdot \left(S_{I_2+\Delta I} + S_{I_3+\Delta I} + S_{I_4+\Delta I}\right) \quad \text{(Eq. 3. 9)}$$

Similarly, the current PSD measured at the central node S_0 can be calculated as

$$S_0 = \left(\frac{\left(\frac{1}{\frac{1}{r_1}+\frac{1}{r_2}+\frac{1}{r_3}+\frac{1}{r_4}}\right)}{\left(\frac{1}{\frac{1}{r_1}+\frac{1}{r_2}+\frac{1}{r_3}+\frac{1}{r_4}}\right)+R_c}\right)^2 \cdot \left(S_{I_1+\Delta I} + S_{I_2+\Delta I} + S_{I_3+\Delta I} + S_{I_4+\Delta I}\right) + \left(\frac{R_c}{\left(\frac{1}{\frac{1}{r_1}+\frac{1}{r_2}+\frac{1}{r_3}+\frac{1}{r_4}}\right)+R_c}\right)^2 \cdot S_{R_c}$$

$$\approx \left(S_{I_1+\Delta I} + S_{I_2+\Delta I} + S_{I_3+\Delta I} + S_{I_4+\Delta I}\right) \qquad \text{(Eq. 3. 10)}$$

Using the equation (Eq. 3. 9) and (Eq. 3. 10), we can eliminate the $S_{I_2+\Delta I}$, $S_{I_3+\Delta I}$, and $S_{Ii4+\Delta I}$, and the S_{I_1} can be written as

$$S_{I_1} = \frac{S_1 - \left(\frac{1}{1+\Delta R\left(\frac{1}{R_2+\Delta R}+\frac{1}{R_3+\Delta R}+\frac{1}{R_4+\Delta R}\right)}\right)^2 \cdot S_0 + \left(\frac{1}{1+\Delta R\left(\frac{1}{R_2+\Delta R}+\frac{1}{R_3+\Delta R}+\frac{1}{R_4+\Delta R}\right)}\right)^2 \cdot \left(\frac{\Delta R}{R_1+\Delta R}\right)^2 \Delta S - \left(\Delta R\left(\frac{1}{R_2+\Delta R}+\frac{1}{R_3+\Delta R}+\frac{1}{R_4+\Delta R}\right)\right)^2 \cdot \Delta S}{1 - \left(\left(\frac{1}{1+\Delta R\left(\frac{1}{R_2+\Delta R}+\frac{1}{R_3+\Delta R}+\frac{1}{R_4+\Delta R}\right)}\right) \cdot \left(\frac{R_1}{R_1+\Delta R}\right)\right)^2} \approx$$

$$\frac{S_1 - \left(\frac{1}{1+\Delta R\left(\frac{1}{R_2+\Delta R}+\frac{1}{R_3+\Delta R}+\frac{1}{R_4+\Delta R}\right)}\right)^2 \cdot S_0 + \left(\frac{\Delta R}{R_1+\Delta R}\right)^2 \Delta S - \left(\Delta R\left(\frac{1}{R_2+\Delta R}+\frac{1}{R_3+\Delta R}+\frac{1}{R_4+\Delta R}\right)\right)^2 \cdot \Delta S}{1 - \left(\left(\frac{1}{1+\Delta R\left(\frac{1}{R_2+\Delta R}+\frac{1}{R_3+\Delta R}+\frac{1}{R_4+\Delta R}\right)}\right) \cdot \left(\frac{R_1}{R_1+\Delta R}\right)\right)^2} \qquad \text{(Eq. 3.11)}$$

Similarly, the S_{I_2}, S_{I_3}, and S_{I_4} can be obtained. Then, using those terms, the equation (Eq. 3. 10) can be rewritten as

$$S_0 = \left\{\left(\frac{R_1}{R_1+\Delta R}\right)^2 S_{I_1} + \left(\frac{\Delta R}{R_1+\Delta R}\right)^2 \Delta S\right\} + \left\{\left(\frac{R_2}{R_2+\Delta R}\right)^2 S_{I_2} + \left(\frac{\Delta R}{R_2+\Delta R}\right)^2 \Delta S\right\}$$
$$+ \left\{\left(\frac{R_3}{R_3+\Delta R}\right)^2 S_{I_3} + \left(\frac{\Delta R}{R_3+\Delta R}\right)^2 \Delta S\right\} + \left\{\left(\frac{R_4}{R_4+\Delta R}\right)^2 S_{I_4} + \left(\frac{\Delta R}{R_4+\Delta R}\right)^2 \Delta S\right\}$$
$$= \left\{\left(\frac{R_1}{R_1+\Delta R}\right)^2 \cdot \left\{\frac{S_1 - \left(\frac{1}{1+\Delta R\left(\frac{1}{R_2+\Delta R}+\frac{1}{R_3+\Delta R}+\frac{1}{R_4+\Delta R}\right)}\right)^2 \cdot S_0 + \left(\frac{\Delta R}{R_1+\Delta R}\right)^2 \Delta S - \left(\Delta R\left(\frac{1}{R_2+\Delta R}+\frac{1}{R_3+\Delta R}+\frac{1}{R_4+\Delta R}\right)\right)^2 \cdot \Delta S}{1 - \left(\left(\frac{1}{1+\Delta R\left(\frac{1}{R_2+\Delta R}+\frac{1}{R_3+\Delta R}+\frac{1}{R_4+\Delta R}\right)}\right) \cdot \left(\frac{R_1}{R_1+\Delta R}\right)\right)^2}\right\} + \left(\frac{\Delta R}{R_1+\Delta R}\right)^2 \Delta S\right\}$$

$$+ \left\{\left(\frac{R_2}{R_2+\Delta R}\right)^2 \cdot \left\{\frac{S_2 - \left(\frac{1}{1+\Delta R\left(\frac{1}{R_1+\Delta R}+\frac{1}{R_3+\Delta R}+\frac{1}{R_4+\Delta R}\right)}\right)^2 \cdot S_0 + \left(\frac{\Delta R}{R_2+\Delta R}\right)^2 \Delta S - \left(\Delta R\left(\frac{1}{R_1+\Delta R}+\frac{1}{R_3+\Delta R}+\frac{1}{R_4+\Delta R}\right)\right)^2 \cdot \Delta S}{1 - \left(\left(\frac{1}{1+\Delta R\left(\frac{1}{R_1+\Delta R}+\frac{1}{R_3+\Delta R}+\frac{1}{R_4+\Delta R}\right)}\right) \cdot \left(\frac{R_2}{R_2+\Delta R}\right)\right)^2}\right\} + \left(\frac{\Delta R}{R_2+\Delta R}\right)^2 \Delta S\right\}$$

$$+ \left\{\left(\frac{R_3}{R_3+\Delta R}\right)^2 \cdot \left\{\frac{S_3 - \left(\frac{1}{1+\Delta R\left(\frac{1}{R_1+\Delta R}+\frac{1}{R_2+\Delta R}+\frac{1}{R_4+\Delta R}\right)}\right)^2 \cdot S_0 + \left(\frac{\Delta R}{R_3+\Delta R}\right)^2 \Delta S - \left(\Delta R\left(\frac{1}{R_1+\Delta R}+\frac{1}{R_2+\Delta R}+\frac{1}{R_4+\Delta R}\right)\right)^2 \cdot \Delta S}{1 - \left(\left(\frac{1}{1+\Delta R\left(\frac{1}{R_1+\Delta R}+\frac{1}{R_2+\Delta R}+\frac{1}{R_4+\Delta R}\right)}\right) \cdot \left(\frac{R_3}{R_3+\Delta R}\right)\right)^2}\right\} + \left(\frac{\Delta R}{R_3+\Delta R}\right)^2 \Delta S\right\}$$

$$+\left\{\left(\frac{R_4}{R_4+\Delta R}\right)^2\cdot\left\{\frac{S_4-\left(\frac{1}{1+\Delta R\left(\frac{1}{R_1+\Delta R}+\frac{1}{R_2+\Delta R}+\frac{1}{R_3+\Delta R}\right)}\right)^2\cdot S_0+\left(\frac{\Delta R}{R_4+\Delta R}\right)^2\Delta S-\left(\Delta R\left(\frac{1}{R_1+\Delta R}+\frac{1}{R_2+\Delta R}+\frac{1}{R_3+\Delta R}\right)\right)^2\cdot\Delta S}{1-\left(\left(\frac{1}{1+\Delta R\left(\frac{1}{R_1+\Delta R}+\frac{1}{R_2+\Delta R}+\frac{1}{R_3+\Delta R}\right)}\right)\cdot\left(\frac{R_4}{R_4+\Delta R}\right)\right)^2}\right\}+\left(\frac{\Delta R}{R_4+\Delta R}\right)^2\Delta S\right\} \quad \text{(Eq. 3. 12)}$$

Note that all of the S_i (i = 0, 1, 2, 3, and 4) values are the measured current PSD at the corresponding nodes, and all R_{is} can be obtained from our numerical method using codes in Agros2D. Therefore, we could obtain the ΔS values like,

$$\Delta S\approx\frac{S_0-\left(\frac{R_1}{R_1+\Delta R}\right)^2\cdot C_{1234}-\left(\frac{R_2}{R_2+\Delta R}\right)^2\cdot C_{2134}-\left(\frac{R_3}{R_3+\Delta R}\right)^2\cdot C_{3124}-\left(\frac{R_4}{R_4+\Delta R}\right)^2\cdot C_{4123}}{\left[\left(\frac{R_1}{R_1+\Delta R}\right)^2\cdot D_{1234}+\left(\frac{\Delta R}{R_1+\Delta R}\right)^2\right]+\left[\left(\frac{R_2}{R_2+\Delta R}\right)^2\cdot D_{2134}+\left(\frac{\Delta R}{R_2+\Delta R}\right)^2\right]+\left[\left(\frac{R_3}{R_3+\Delta R}\right)^2\cdot D_{3124}+\left(\frac{\Delta R}{R_3+\Delta R}\right)^2\right]+\left[\left(\frac{R_4}{R_4+\Delta R}\right)^2\cdot D_{4123}+\left(\frac{\Delta R}{R_4+\Delta R}\right)^2\right]}$$

(Eq. 3. 13)

The C_{ijkl}, and D_{ijkl} in the equation (Eq. 3. 13) were defined as

$$C_{ijkl}\equiv\left\{\frac{S_i-\left(\frac{1}{1+\Delta R\left(\frac{1}{R_j+\Delta R}+\frac{1}{R_k+\Delta R}+\frac{1}{R_l+\Delta R}\right)}\right)^2\cdot S_0}{1-\left(\frac{R_i}{R_i+\Delta R}\right)^2}\right\} \quad \text{(Eq. 3. 14)}$$

$$D_{ijkl}\equiv\left\{\frac{\left(\frac{\Delta R}{R_i+\Delta R}\right)^2-\left(\frac{\Delta R}{R_j+\Delta R}+\frac{\Delta R}{R_k+\Delta R}+\frac{\Delta R}{R_l+\Delta R}\right)^2}{1-\left(\frac{R_i}{R_i+\Delta R}\right)^2}\right\} \quad \text{(Eq. 3. 15)}$$

Note that since the ΔS is the current PSD originated from the ΔR, the ΔS can be considered as the current PSD ΔS_I coming from the segment located at the *node* 0. Then, from the equation (Eq. 3. 7), we can calculate the effective noise source density n_{eff} as

$$n_{eff}(x,y)=\frac{(\Delta C)^2}{(I_0)^2}\frac{f}{kT}\cdot\frac{\Delta S(f,x,y)}{\Delta x\Delta y} \quad \text{(Eq. 3. 16)}$$

Here, the ΔC and I_0 represent *the number of charge carriers in the area of* $(\Delta l)^2$ and *the measured current at the node 0*, respectively.

3.6 Experimental Setup for SNM

3.6.1 CNT Network Sample Preperation

First, semiconducting CNTs or metallic CNTs (NanoIntegris Inc.) were dispersed in a 1, 2-dichlorobenzene solution (0.01 mg/mL). Second, the CNT solution was dropped on a clean SiO_2 substrate for 1 min (oxide thickness~ 300 nm). Third, the CNTs adsorbed SiO_2 substrate was rinsed with a 1, 2-diclorobenzene solution. Lastly, a Ti/Au (15/40 nm) electrode was fabricated on the substrate via a thermal evaporation method through a shadow mask.

Also, we fabricated a cross-patterned CNT network by repeating a photolithography method twice. First, semiconducting CNTs and metallic CNTs (NanoIntegris Inc.) were dispersed in 1, 2-dichlorobenzene solutions (0.01 mg/mL), respectively. Second, a line pattern (photoresist line width 20 μm, bare SiO_2 line width 4 μm) of photoresist film (AZ5214-E, Clariant Inc.) was fabricated via a photolithography method. Third, the photoresist coated SiO_2 substrate was dipped into the metallic CNT solution for 1 min. Fourth, the metallic CNT adsorbed substrate was rinsed with a 1, 2-dichlorobenzen

solution. Fifth, the substrate was dipped into an acetone solution. Here, the photoresist layer was developed and only the line-pattern of metallic CNT networks was remained on the substrate. Sixth, a line pattern (photoresist line width 20 μm, SiO_2 line width 4 μm) of photoresist film was fabricated via a photolithography method. Here, the direction of the line-pattern of the photoresist film is orthogonal to the direction of metallic CNT networks. Seventh, the substrate was dipped into the semiconducting CNT solution for 1 min. Eighth, the substrate was rinsed with a 1, 2-dichlorobenzen solution. Ninth, the substrate was dipped into an acetone solution. Here, the photoresist layer was developed and only the cross-patterned semiconducting CNT networks and metallic CNT networks were remained on the substrate. Lastly, a Ti/Au (15/40 nm) electrode was fabricated on the cross-patterned CNT network via a thermal evaporation method through a shadow mask. Here, the electrode is orthogonally connected with metallic CNT networks.

3.6.2 Noise Measurement

Fig. 3. 5 shows a schematic diagram depicting the experimental setup for the noise measurement. We utilized a conducting AFM system (XE-70, Park Systems) with a Pt coated conducting AFM probe (PPP-CONTSCPt, Park Systems). Then, we contacted the AFM probe to the surface of CNT networks and applied a DC bias to the electrode. Then, we converted output

currents to amplified voltage signals by a low-noise preamplifier (SR570, Stanford Research Systems) and measured the PSD by a homemade spectrum analyzer [36]. Note that the homemade spectrum analyzer has a band-pass filter and a RMS-DC converter (AD737 Chip, Analog Devices) functions. By using the band-pass filter included preamplifier SR 570, we measured the signal within the frequency of interests. Lastly, we measured the PSD signals by dividing the converted DC signals by the bandwidth of filters.

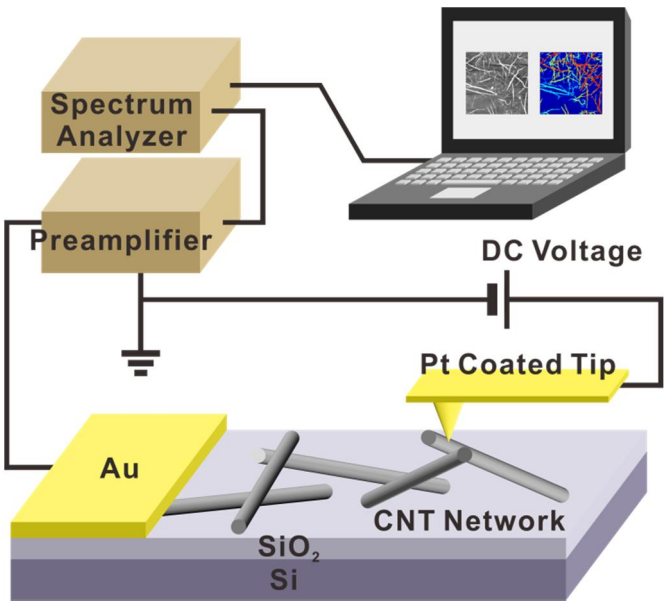

Fig. 3. 5 Schematic diagram depicting the experimental setup for the noise measurement.

3.7 Result and Discussion

3.7.1 Noise Source imaging of a Metallic Carbon Nanotube Network

Fig. 3. 6 (a) shows the topographic image of a metallic CNT network. The topographic image was measured using a contact mode AFM. Contact force between a probe and the CNT network was 0.2 nN. The bias voltage of 0.1 V was applied to the AFM probe. The scan rate was 0.5 Hz. The diameters of CNTs and bundles are 1.3~1.7 and about 10 nm, respectively.

Fig. 3 6 (b) shows the gate profile of the metallic CNT network. To measure the gate profile, current maps of the CNT network were measured by changing a gate bias voltage. Further, we plotted a gate profile at a specific contact point using the current values in the current maps. The contact point on the CNT network is marked by (A) in Fig. 3. 6 (a). During the conducting AFM measurements, the 0.1 V of bias voltage was applied to the probe. The gate profile shows a constant value. This indicates that the CNT network is metallic.

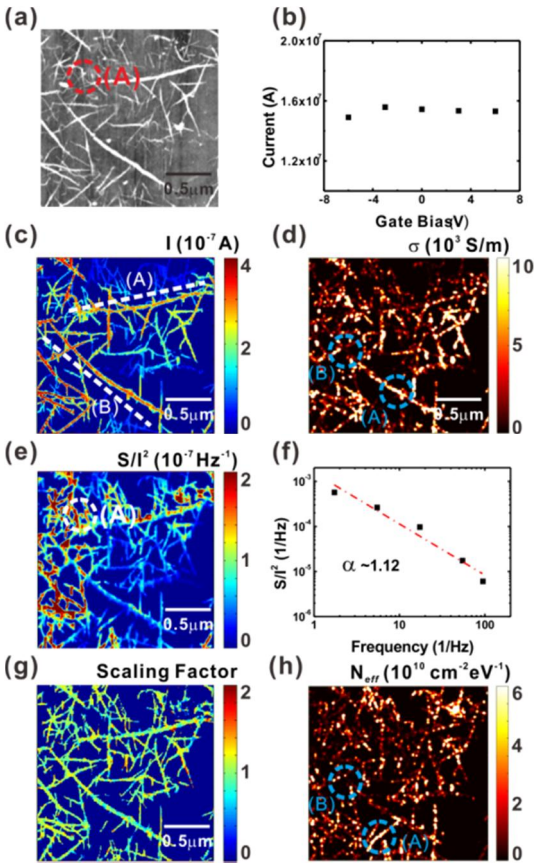

Fig. 3. 6 Noise source imaging on a metallic CNT network. (a) AFM topography image of a metallic CNT network. (b) Gate profile of a metallic CNT network. The metallic CNT network shows no dependence on a gate bias. (c) Current image of the metallic CNT network. The bias voltage of 0.1 V was applied to the metallic CNT network. (d) Conductivity map of the metallic CNT network. (e) Current-normalized noise PSD map (center frequency ~54.77 Hz) of the metallic CNT network. (f) The graph of current-normalized noise PSD versus frequency at the point (a) in Fig. 3. 6 (e). (g) Scaling factor map of the metallic CNT network. The metallic CNT shows 1/*f* noise behavior at all scanned region. (h) Noise source density of the metallic CNT network. The noise source density map was calculated from the PSD map and the conductivity map of the metallic CNT network.

Fig. 3. 6 (c) shows the current map of the metallic CNT network. The bias voltage of 0.1 V was applied to a probe and no gate bias was applied. The current map was well matched with the topographic map in

Fig. 3. 6 (a). For CNTs that are in contact with many other CNTs such as bundles (A) and (B), the number of current paths increased and showed high currents. In contrast, the end portions of the CNT network showed rather low current values because the number of current path is lower than other regions.

Fig. 3. 6 (d) shows the conductivity map of the metallic CNT network. To estimate the conductivity $\sigma(x, y)$ at each point from the measured $I(x, y)$ values, we developed an iterative method in a previous paper based on a computational algorithm coded in Agros2D (http://agros2d.org) [15]. The conductivity value at the point A of a bundle (marked by (A)) is 553.2 S/m. And the conductivity value at the point B of same bundle (marked by (B)) is 1.04×10^4 S/m. The conductivity at the B point of the bundle is higher than the conductivity at the A point. Presumably, In the case of the point A, the conductivity seems to low due to a contact resistance at CNT junctions. This result clearly shows that our method can be apply for the measurement of conductivities on two-dimensional nano devices.

Fig. 3. 6 (e) shows the current-normalized PSD S_I/I^2 map of the metallic CNT networtk measured at 54.77 Hz. The scanned area is same with the current map at Fig. 3. 6 (c). Note that, the topography, the current map and the current noise PSD map were measured simultaneously. The measured PSD shows high values at dense region of the CNT network.

Further, the PSD shows much lower value at low-CNT density region or at the end portion of CNT network. The PSD values showed no dependence with the diameters of CNTs. This indicates that the noise activity of a CNT network is depending on the density of CNTs in a metallic CNT network. Presumably, when the density of a CNT network near a measured point is high, a noise value will be affected by noise sources present in various current paths. Thus, the measured PSD value appears to be closely related to a CNT network density.

Fig. 3. 6 (f) shows the graph of the scaling behavior of a metallic CNT network. To measure the scaling behavior, current noise PSD maps were measured on the same area of the CNT network by changing the center frequency of a band pass filter. The center frequencies of measured PSD maps are 1.732, 5.477, 17.32, 54.77 and 94.87 Hz. Then, we plotted the scaling behavior graph using the PSD values at a specific point in the scanned area. The specific contact point on the CNT network is marked by (A) in Fig. 3. 6 (a) and (e). The scaling behavior graph shows a typical $1/f$ noise behavior. A slope of the fitting curve was estimated as ~1.12.

By using a calculated scaling factor, we can make more in-depth analysis on the noise of an electronic device. The most common theoretical model for analyzing noise is a number fluctuation model. [1, 7, 26-29] From the number fluctuation model, the PSD shows a $1/f$ scaling behavior when

individual noise sources trap and release charge carriers with different relaxation times. Also, The PSD shows a $1/f^2$ scaling behavior if the channel has a dominant noise source [37, 38]. In the actual experiment of graphene analysis by a NSI method, we could investigate the noise source just below an AFM probe by measuring a local scaling factor [15]. In this paper, we calculated the scaling factor map of metallic CNT network to analyze the noise sources.

Fig. 3. 6 (g) shows the scaling factor map of the metallic CNT network. To estimate the scaling factor map, we measured the current noise PSD maps on the same area of the metallic CNT network by changing the center frequency of a band pass filter. The center frequencies of measured PSD maps are 1.732, 5.477, 17.32 and 54.77 Hz. Then, we calculated the scaling factor of each point in the scanned area. The scaling factor values show values similar to 1 at most points in the scanned area. This indicates that the metallic CNT have no dominant noise sources.

In the previous papers, the researchers suggested that the main reason of current noises of CNT devices is noise traps in current paths. Here, we calculated the noise source density of the metallic CNT network via Wiener-Khintchine theorem and a differential analysis [39]. We defined an effective noise source density neff in the small segment of a CNT network in the area of $\Delta x \Delta y$ as [15]

Here, ΔC, I, f, k, T and ΔS_I are a number of charge carriers, an electrical current, a frequency, Boltzmann constant, a temperature and the PSD of a current noise generated by the segment $\Delta x \Delta y$, respectively. The ΔS_I is calculated by the resistance network model [15]

$$n_{eff}(f,x,y) = \frac{(\Delta C)^2}{(I)^2}\frac{f}{kT}\cdot\frac{\Delta S_I(f,x,y)}{\Delta x \Delta y} \qquad \text{(Eq. 3. 17)}$$

Fig. 3. 6 (h) shows the noise source density map of the metallic CNT network. Here, we utilized the current noise PSD at the center frequency of 54.77 Hz to estimate the noise source density map. The estimated n_{eff} value at a bundle (region (i), diameter ~ 12 nm) is 4.423 x 10^8 $cm^{-2}eV^{-1}$. And, the estimated n_{eff} value at a thin CNT (region (ii), diameter ~ 1.5 nm) is 2.012 x 10^{11} $cm^{-2}eV^{-1}$. This indicates that the n_{eff} at a CNT bundle is much lower than that of a single CNT. This result can explain by a screening behavior of charge traps in an oxide layer. In our experiment, noise sources can exist in a SiO_2 layer as well as in CNTs itself. In the case of thick CNT bundles, CNTs at the bottom side of bundles can screen SiO_2 traps from charge carriers in CNTs at the top side of bundles, and the effect of SiO_2 traps could be reduced. In this case, the total effective noise source density at a thick CNT bundle could appear lower than those at a thin bundle or a single CNT. Similar effect in the case of a graphene was reported previously [15, 40, 41].

3.7.2 Noise Source imaging of a Semiconducting Carbon Nanotube Network

Fig. 3. 7 (a) shows the current map of a semiconducting CNT network. The set point and the scan rate of an AFM were 0.2 nN and 0.7 Hz. The bias voltage of 2 V was applied to an AFM probe. Using the current map, we can clearly distinguish individual CNTs. This indicates that, we successfully performed a conducting-AFM measurement on the semiconducting CNT network.

Fig. 3. 7 (b) shows the gate profile of the semiconducting CNT network. To measure the gate profile, conducting AFM measurements were performed by changing gate bias on the same area of the CNT network. Further, we plotted the gate profile using the current at a specific point in the scanned area. The specific contact point on the CNT network is marked by (i) in Fig. 3. 7 (a). During the AFM measurements, the bias voltage of 2 V was applied to an AFM probe. The gate profile shows a p-type semiconducting behavior. This indicates that we successfully assembled semiconducting CNTs on a SiO_2 substrate.

Fig. 3. 7 (c) shows a conductivity map of the semiconducting CNT network. We used an iterative method to calculate the conductivity map of the semiconducting CNT network. The conductivity of a thin CNT (marked

by (A)) is 14.8 S/m and the conductivity of CNT bundle (marked by (B)) is 203.2 S/m. The conductivity values of the semiconducting CNT network were measured lower than the conductivity values of the metallic CNT network at figure 2.

Using the conductivity map, we were able to calculate the mobility map of the semiconducting CNT network. Fig. 3. 7 (d) shows the mobility map of the semiconducting CNT network. To calculate the mobility map, we estimated the conductivity map at different gate biases of -6, -3, 0, 3 and 6 V. Then, we calculated the field-effect mobility values at each point in the map by a following equation [42].

$$\mu = \frac{t}{C_0} \cdot \frac{d}{dV_g}(\sigma) \qquad \text{(Eq. 3. 18)}$$

Where t, C_0, V_g and σ represent the thickness of a CNT, a gate capacitance per unit channel area, a gate bias and a conductivity, respectively. The calculated mobility values at the dark regions are about 100 ~ 500 $cm^2/V{\cdot}s$. And, the calculated mobility values at bright regions are over 5000 $cm^2/V{\cdot}s$. Note that the measured mobility values of CNT networks on previous papers are lower than the single CNT based devices [42-46] This result implies that the some regions of a CNT network have their intrinsic mobility characteristic of a single CNT, even though the averaged mobility is much lower than the mobility of a single CNT.

Fig. 3. 7 (e) shows the graph of a correlation between mobilities and the conductivities of the semiconducting CNT network at a 0 gate bias. Using the conductivity map at a 0 gate bias and the mobility map, we plotted a scatter graph with mobilities as x coordinates and conductivities as y coordinates. The graph shows no correlation between mobilities and the conductivities.

Fig. 3. 7 (f) shows the graph of a correlation between mobilites and conductivities of the semiconducting CNT network at a gate bias of -3 V. Here, unlike the case of a 0 gate bias, conductivities at a -3 V gate bias and mobilities are linearly proportional. This result implies that mobility values are also high at high conductivity regions.

Also, we measured a current noise PSD map while measuring the topography and current map of the semiconducting CNT network. Fig. 3. 7 (g) shows the graph of current-normalized noise PSD value versus center frequency. Here, back and red dots represent PSD values when an AFM probe was in contact with a CNT surface (marked by (A) in Fig. 3. 7 (a) and (h)) and a crossed-CNT junction (marked by (B) in Fig. 3. 7 (a) and (h)). The current noise PSD shows a typical $1/f$ noise behavior when an AFM probe was contacted with the CNT surface. It indicates that a number of noise sources existing in current paths. In contrast, in the case of a crossed-CNT junction contact, the current noise PSD shows a $1/f^2$ behavior at a rather

low-frequency condition near or below ~10 Hz. This indicates that there exist noise sources in a direct contact with a conducting probe at the CNT junctions [37, 38]. This results seem to be related with the mechanical deformation phenomena of a upper CNT at a crossed-CNT junction [47]. It was previously reported that the top CNT of crossed-CNTs were locally bent at a junction of crossed-CNTs. In theoretical investigation, as the top CNT of a crossed-CNT is mechanically deformed, the energy levels are generated inside the band gab of the top CNT that was not present before a mechanical deformation. Presumably, the energy levels can be act as noise sources at a crossed-CNT junction. Note that our AFM probe doesn't appear to produce radial deformation during conducting AFM measurements because of weak contact pressures (102~255 kPa, depend on the set point of an AFM probe) [48]. Note that, these $1/f^2$ noises decayed quickly compare to $1/f$ noises as a frequency increased. Thus we could observe a $1/f$ noise behavior at a high-frequency condition.

Using the current noise PSD values at different frequencies, we could calculate the scaling factor map of the semiconducting CNT network. Fig. 3. 7 (h) shows the scaling factor map of a semiconducting CNT network. The values of each point in the map are the scaling factors of noise PSD values at each point. Note that, for fitting curve calculations, only the PSD values measured under a frequency less than 30 Hz were used to avoid a $1/f$

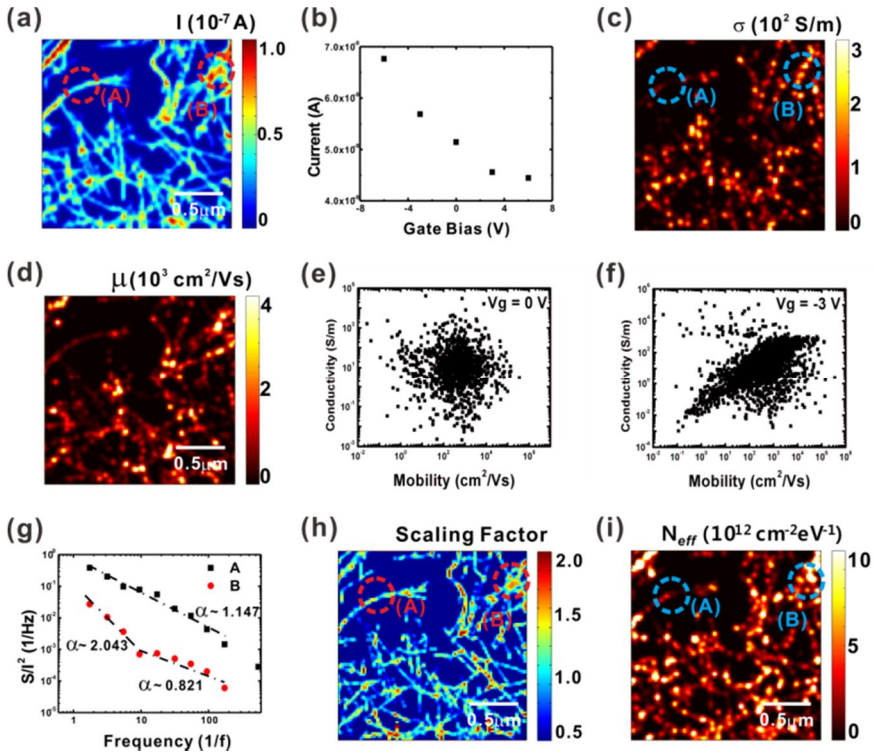

Fig. 3. 7 Noise source imaging on a semiconducting CNT network. (a) Current image of the semiconducting CNT network. The bias voltage of 2 V was applied to the semiconducting CNT network. (b) Gate profile of the semiconducting CNT network. The semiconducting CNT network shows a p-type behavior. (c) Conductivity map of the semiconducting CNT network. (d) mobility map of the semiconducting CNT network. The mobility map was calculated by conductivity maps at different gas biases. (e) Scatter graph of correlation between conductivity at 0 gate bias and mobility. (f) Scatter graph of correlation between conductivity at -3 gate bias and mobility. The mobility of semiconducting CNT network is linearly proportion to the on-state conductivity of semiconducting CNT network. (g) The graph of current-normalized noise PSD versus frequency at CNT junction (red dot) and surface of CNT (black dot). (h) Scaling factor map of the semiconducting CNT network. The semiconducting CNT shows 1/f2 noise behavior at semiconducting CNT junctions. (i) Noise source density of the semiconducting CNT network.

behavior at a high frequency condition. The calculated scaling factors were close to 1 in most scanned area of the semiconducting CNT network. But at

the CNT junctions, the scaling factors were estimated to be close to 2. This indicates that there exist dominant noise sources at CNT junctions [38, 39].

Fig. 3. 7 (i) shows the calculated map of the noise source density of the semiconducting CNT network. Here, we utilized the current noise PSD map at the center frequency of 54.77 Hz. Unlike the case of metallic CNT, the semiconducting CNT network shows high noise trap densities at the junctions of the semiconducting CNT network. The n_{eff} at the surface of a CNT (marked by (A) in the Fig. 3. 7 (i)) is 3.98 x 10^{11} $cm^{-2}eV^{-1}$. And, the n_{eff} at a CNT junction (marked by (B) in the Fig. 3. 7 (i)) is 2.15 x 10^{12} $cm^{-2}eV^{-1}$. This indicates that, a lot of current noises can be generated at semiconducting CNT junctions.

3.7.3 Noise Source imaging of a Cross-patterned Carbon Nanotube Network

Fig. 3. 8 (a) shows the topographic image of a cross-patterned CNT network. The topographic image was measured via a contact mode AFM. A contact force between a probe and the CNT network was 0.5 nN. The scan rate was 0.05 Hz. Here, metallic CNTs were assembled in an x-axis direction. And semiconducting CNTs were assembled in a y-axis direction. The electrode was connected with metallic CNT networks. The widths of horizontally and vertically assembled CNT networks are 4 μm. To selectively

assemble the CNTs on specific areas, we used a conventional photolithography method. The AFM image clearly shows that the cross-patterned CNT network was successfully fabricated.

Fig. 3. 8 (b) shows the current map of the cross-patterned CNT network. To measure the current image of a scanned area, the bias voltage of 1 V was applied to an AFM probe. A metallic CNT assembled area shows much higher current values than those of a semiconducting CNT assembled area. From the result, we can expect that the conductivities of a metallic CNT network will be higher than those of a semiconducting CNT network.

Fig. 3. 8 (c) shows the calculated conductivity map of the cross-patterned CNT network. The conductivity map was calculated via an iterative method. The conductivity values of a metallic CNT adsorbed region were much higher than those of a semiconducting CNT network adsorbed region as we expected. The averaged conductivity of a metallic CNT adsorbed area is 1.963 x 10^3 S/m. And the averaged conductivity of a semiconducting CNT adsorbed area is 1.325 x10^3 S/m. The conductivity map allowed us to compare the conductivity values on specific regions by expressing in a single image.

Fig. 3. 8 (d) shows the map of scaling factors of the cross-patterned CNT network. To calculate the scaling factor, we used noise PSD maps at the center frequencies of 1.732, 3.162, 17.32 and 54.77 Hz. The scaling factor

map showed a value similar to 1 at a metallic CNT adsorbed area. And, the scaling factor map showed a value similar to 2 at some points in a semiconducting CNT adsorbed area and a metallic-semiconducting crossed area. This result clearly shows that there exist dominant noise sources in a semiconducting CNT network.

Fig. 3. 8 (e) shows the current noise PSD of the cross-patterned CNT network. The center frequency of a band pass filter is 17.32 Hz. The averaged PSD value of a metallic CNT adsorbed region is 2.21 x 10^{-4} Hz^{-1}. And the averaged PSD of a semiconducting CNT assembled region is 2.68 x 10^{-4} Hz^{-1}. The high PSD values indicate that there are many noise sources near the measured points.

Fig. 3. 8 (f) shows the noise source density map of the cross-patterned CNT network. Here, we utilized the current noise PSD map at the center frequency of 17.32 Hz. The calculated noise source density showed clear difference between a metallic CNT adsorbed area and a semiconducting CNT adsorbed area. The averaged noise trap density of the metallic CNT adsorbed area is 3.95 x 10^{11} $cm^{-2}eV^{-1}$. And the averaged noise trap density of the semiconducting CNT adsorbed area is 5.53 x 10^{11} $cm^{-2}eV^{-1}$. This indicates that a semiconducting CNT network generates more noises than a metallic CNT network.

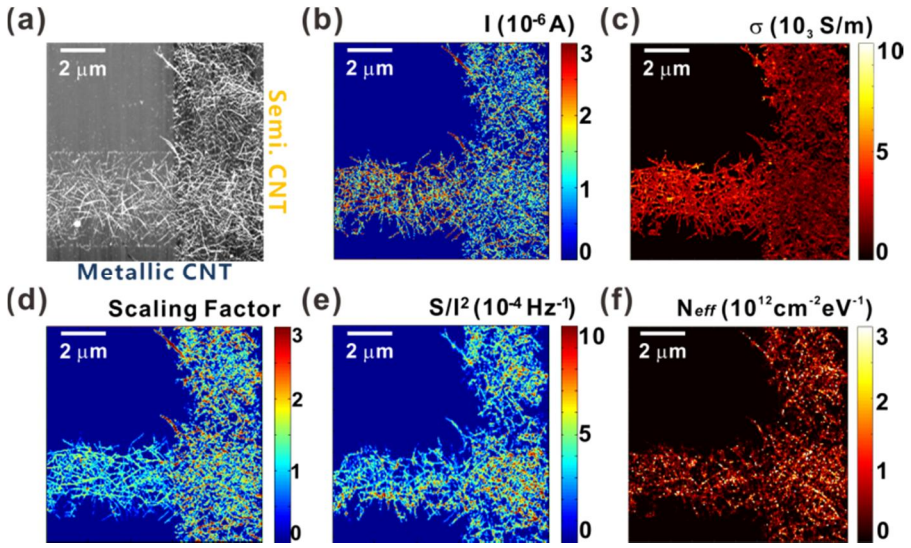

Fig. 3. 8 Noise source imaging on a cross-patterned CNT network. (a) AFM topography image of a cross-patterned CNT network. (b) Current image of the cross-patterned CNT network. The bias voltage of 1 V was applied to the cross-patterned CNT network. (c) Conductivity map of the cross-patterned CNT network. (d) Scaling factor map of the cross-patterned CNT network. Some semiconducting CNT adsorbed region shows $1/f^2$ noise behavior. (e) Current-normalized noise PSD map (center frequency ~17.32 Hz) of the cross-patterned CNT network. (f) Noise source density of the cross-patterned CNT network.

3.8 Summary

In summary, we have investigated the local noise of CNT networks via a NSI method. In this method, the conducting AFM probe was directly contacted with CNT networks, and the current maps and the noise PSD maps of CNT networks were measured. The measured maps were analyzed to calculate conductivity maps, mobility maps, scaling factor maps and noise source density maps. We found that the noise of a CNT network was

depending on the density of a CNT network and diameters of CNTs. Also, in the case of a semiconducting CNT network, we found that a large amount of noise occurs at CNT junctions. Additionally, we compared the noise characteristics of a metallic CNT network and a semiconducting CNT network by fabricating a cross-patterned CNT network of a metallic CNT networks and a semiconducting CNT networks. Our researches can be a guideline in the basic study of noises and the applications of CNT based devices.

References

[1] F. N. Hooge, T. G. M. Kleinpenning, L. K. J. Vandamme, Experimental Studies on 1-F Noise. *Rep. Prog. Phys.* **44**, 479-532 (1981).

[2] G. Ghibaudo, O. Roux, C. Nguyenduc, F. Balestra, J. Brini, Improved Analysis of Low-Frequency Noise in Field-Effect Mos-Transistors. *Phys. Stat. Sol. (a)* **124**, 571-581 (1991).

[3] M. G. Sung et al., Scanning Noise Microscopy on Graphene Devices. *Acs Nano* **5**, 8620-8628 (2011).

[4] D. M. Fleetwood, N. Giordano, Direct Link between 1/F Noise and Defects in Metal-Films. *Phys. Rev. B* **31**, 1157-1160 (1985).

[5] T. G. M. Kleinpenning, Low-Frequency Noise in Schottky-Barrier Diodes. *Solid State Electron.* **22**, 121-128 (1979).

[6] F. V. Farmakis et al., Low frequency noise in Schottky barrier contacts of titanium nitride on n-type silicon. *Semicond. Sci. Tech.* **13**, 1284-1289 (1998).

[7] S. Christensson, I. Lundstrom, C. Svensson, Low Frequency Noise in Mos Transistors .I. Theory. *Solid State Electron.* **11**, 797-812 (1968).

[8] C. Surya, T. Y. Hsiang, Surface Mobility Fluctuations in Metal-Oxide-Semiconductor Field-Effect Transistors. *Phys. Rev. B* **35**, 6343-6347 (1987).

[9] S. Soliveres, J. Gyani, C. Delseny, A. Hoffmann, F. Pascal, 1/f noise and percolation in carbon nanotube random networks. *Appl. Phys. Lett.* **90**, 082107 (2007).

[10] A. A. Balandin, Low-frequency 1/f noise in graphene devices. *Nat. Nanotechnol.* **8**, 549-555 (2013).

[11] I. Heller et al., Charge Noise in Graphene Transistors. *Nano Lett.* **10**, 1563-1567 (2010).

[12] M. Briman, K. Bradley, G. Gruner, Source of 1/f noise in carbon nanotube devices. *J. Appl. Phys.* **100**, 013505 (2006).

[13] Y. M. Lin, J. Appenzeller, J. Knoch, Z. H. Chen, P. Avouris, Low-frequency current fluctuations in individual semiconducting single-wall carbon nanotubes. *Nano Lett.* **6**, 930-936 (2006).

[14] Y. M. Lin, J. C. Tsang, M. Freitag, P. Avouris, Impact of oxide substrate on electrical and optical properties of carbon nanotube devices. *Nanotechnology* **18**, 295202 (2007).

[15] H. Lee et al., Nanoscale Direct Mapping of Noise Source Activities on Graphene

Domains. *Acs Nano* **10**, 10135-10142 (2016).

[16] P. G. Collins, M. S. Fuhrer, A. Zettl, 1/f noise in carbon nanotubes. *Appl. Phys. Lett.* **76**, 894-896 (2000).

[17] W. J. Kong, L. Lu, D. L. Zhang, Z. W. Pan, The 1/f noise in multiwalled carbon nanotubes. Chinese Phys 14, 2090-2092 (2005).

[18] Y. M. Lin, J. Appenzeller, Z. H. Chen, P. Avouris, Electrical transport and 1/f noise in semiconducting carbon nanotubes. *Physica E* **37**, 72-77 (2007).

[19] S. Reza, Q. T. Huynh, G. Bosman, J. Sippel-Oakley, A. G. Rinzler, Thermally activated low frequency noise in carbon nanotubes. *J. Appl. Phys.* **99**, 114309 (2006).

[20] G. X. Liu, S. Rumyantsev, M. S. Shur, A. A. Balandin, Origin of 1/f noise in graphene multilayers: Surface vs. volume. *Appl. Phys. Lett.* 102, 093111 (2013).

[21] A. A. Kaverzin, A. S. Mayorov, A. Shytov, D. W. Horsell, Impurities as a source of 1/f noise in graphene. *Phys. Rev. B* **85**, 075435 (2012).

[22] A. N. Pal et al., Microscopic Mechanism of 1/f Noise in Graphene: Role of Energy Band Dispersion. *Acs Nano* **5**, 2075-2081 (2011).

[23] G. Y. Xu et al., Effect of Spatial Charge Inhomogeneity on 1/f Noise Behavior in Graphene. *Nano Lett.* **10**, 3312-3317 (2010).

[24] C. J. Delker, S. Kim, M. Borg, L. E. Wernersson, D. B. Janes, 1/f Noise Sources in Dual-Gated Indium Arsenide Nanowire Transistors. *IEEE T. Electron Dev.* **59**, 1980-1987 (2012).

[25] N. K. Rajan, D. A. Routenberg, J. Chen, M. A. Reed, 1/f Noise of Silicon Nanowire BioFETs. *IEEE Electr. Device L.* **31**, 615-617 (2010).

[26] A. L. Mcwhorter, Surface Traps and 1-F Noise in Germanium. *Phys. Rev.* **98**, 1191-1192 (1955).

[27] C. H. Suh, Carrier Number Fluctuation Model of 1/F Noise in a Semiconductor-Device. *IEEE T. Electron Dev.* **34**, 906-910 (1987).

[28] G. Ghibaudo, On the Theory of Carrier Number Fluctuations in Mos Devices. *Solid State Electron.* **32**, 563-565 (1989).

[29] A. Corradetti et al., Evidence of Carrier Number Fluctuation as Origin of 1/F Noise in Polycrystalline Silicon Thin-Film Transistors. Appl Phys Lett 67, 1730-1732 (1995).

[30] P. Dutta, P. M. Horn, Low-Frequency Fluctuations in Solids - 1-F Noise. *Rev. Mod. Phys.* **53**, 497-516 (1981).

[31] F. N. Hooge, 1-F Noise. Physica B & C 83, 14-23 (1976). [20] R. V. Seidel et al., Sub-

20 nm short channel carbon nanotube transistors. Nano Lett 5, 147-150 (2005).

[32] F. N. Hooge, 1/F Noise Is No Surface Effect. *Phys. Lett. A* **29**, 139-140 (1969).

[33] K. I. Bolotin et al., Ultrahigh electron mobility in suspended graphene. *Solid State Commun.* **146**, 351-355 (2008).

[34] T. Mitsuhashi, K. Yoshida, A Resistance Calculation Algorithm and Its Application to Circuit Extraction. *IEEE T. Comput Aid. D.* **6**, 337-345 (1987).

[35] J. G. P. Barnes, An Algorithm for Solving Non-Linear Equations Based on the Secant Method. *Comput. J.* **8**, 66-72 (1965).

[36] M. Engelson, Modern Spectrum Analyzer Theory and Applications. *Artech House: Norwood*, (1984).

[37] P. Magnone et al., 1/f Noise in Drain and Gate Current of MOSFETs With High-k Gate Stacks. *IEEE T. Device Mat. Re.* **9**, 180-189 (2009).

[38] K. S. Jeong et al., Crystal Quality Effect on Low-Frequency Noise in ZnO TFTs. *IEEE Electr. Device L.* **32**, 1701-1703 (2011).

[39] S. Kogan, Electronic Noise and Fluctuations in Solids. *Cambridge Univ. Press: Cambridge*, (1996).

[40] Y. M. Lin, P. Avouris, Strong suppression of electrical noise in bilayer graphene nanodevices. *Nano Lett.* **8**, 2119-2125 (2008).

[41] Y. Sui, J. Appenzeller, Screening and Interlayer Coupling in Multilayer Graphene Field-Effect Transistors. *Nano Lett.* **9**, 2973-2977 (2009).

[42] M. Lee et al., "Textured" Network Devices: Overcoming Fundamental Limitations Limitations of Nanotube/Nanowire Network-Based Devices. *Small* **5**, 1642-1648 (2009).

[43] X. S. Wang et al., Fabrication of Ultralong and Electrically Uniform Single-Walled Carbon Nanotubes on Clean Substrates. *Nano Lett.* **9**, 3137-3141 (2009).

[44] T. Durkop, S. A. Getty, E. Cobas, M. S. Fuhrer, Extraordinary mobility in semiconducting carbon nanotubes. *Nano Lett.* **4**, 35-39 (2004).

[45] J. Kim et al., Large Scale Assembly of Pristine Semiconducting Carbon Nanotube Network-Based Devices Exhibiting Intrinsic Characteristics. *J. Phys. Chem. C* **117**, 19721-19728 (2013).

[46] J. Lee et al., Floating electrode transistor based on purified semiconducting carbon nanotubes for high source-drain voltage operation. *Nanotechnology* **23**, 085204 (2012).

[47] A. Nojeh, G. W. Lakatos, S. Peng, K. Cho, R. F. W. Pease, A carbon nanotube cross structure as a nanoscale quantum device. *Nano Lett.* **3**, 1187-1190 (2003).

[48] A. K. Naieni, P. Yaghoobi, D. J. Woodsworth, A. Nojeh, Structural deformations and current oscillations in armchair-carbon nanotube cross devices: a theoretical study. *J. Phys. D*: *Appl. Phys.* **44**, 085402 (2011).

Chapter 4.
CNT-dye Hybrid Structure for Gas Sensor Application

4.1 Introduction

Selective gas sensors have been widely used to alarm the leakage of hazardous gases in living environments and industrial complexes [1-15]. One example can be a colorimetric gas sensor, where colorimetric dye molecules on a solid substrate react with specific gas species and exhibit colour changes as a sensing signal [9-12]. Colorimetric gas sensors are usually very cheap and allow one to selectively detect a broad range of different gas species. However, they have some disadvantages such as a rather slow response time and a low sensitivity. Also, colorimetric gas sensors cannot be used to quantitatively evaluate gas concentrations. On the other hand, electrochemical gas sensors have been utilized for the fast and quantitative evaluation of specific hazardous gas species [13-15]. However, electrochemical sensors are rather expensive and can be used only for limited gas species. Recently, semiconducting channels based on various nanostructures have been utilized to build cheap and selective gas sensors for

the sensitive and fast evaluation of hazardous gas species [1-8]. However, such nanostructure-based sensors often rely on rather non-specific interactions between gas molecules and nanostructure surfaces. Thus, they usually exhibited a rather poor selectivity. In addition, some environmental conditions such as humidity can unpredictably affect their sensing signals, which makes it very difficult to use them for the quantitative evaluation of gas concentrations. Moreover, many of such sensors require a heat treatment to refresh used sensors for repeated measurements.

Herein, we built a hybrid nanostructure of colorimetric dye-functionalized sol-gel matrix on carbon nanotubes to develop refreshable and flexible gas sensors for selective and quantitative sensing. In this sensor, the selective and reversible binding of target gas molecules onto colorimetric dye in the sol-gel matrix caused ion density changes on the layer, which was measured by an underlying semiconducting carbon nanotube-based transistor. Hazardous gas species with a concentration below its permissible exposure limit caused the large conductance change of a CNT-dye hybrid gas sensor more than 50% of its original conductance. It is presumably because a sol-gel matrix provides an ideal environment for the selective gas-dye reactions and the electrical signal transduction by a CNT device. To show the versatility of our strategy, we built gas sensors with different dyes to selectively detect various hazardous gases such as SO2, NH3 and Cl2.

Significantly, the sensor signals were recovered back to its original values without any heat treatment when the target gas was removed. Furthermore, the sensor signals exhibited a rather simple linear dependence to the environmental humidity conditions, enabling the calibration of our sensor signals under different humidity conditions. Since our sensors provide a large signal and can be refreshable without any high temperature treatment, it can be an ideal device for versatile practical applications such as hazardous gas monitoring in public areas and industrial complexes.

4.2 Fabrication Process of a CNT-dye hybrid Gas Sensor and Its Sensing Mechanism

4.2.1 Synthetic Method for Sol-Gel Metrix

We used Soslick group's method to fabricate dye-functionalized sol-gel matrixes [9]. First, we combined Tetraethoxysilane, triethoxy(octyl)silane, HCl (0.1 M aqueous), 2-methoxyethanol, propylene glycol monomethyl ether acetate, and DI water were combined in a molar ratio of 1:1:0.01:11:5:19 to make a ormosil solution and, added surfactant (Cetylpyridinium chloride, 1%/vol.) to assist in surface wetting. Next, we stirred the ormosil solution for 4 hours at 60 ℃. Then, we mixed with dye

molecules (methy red or chlorophenol red) and the ormosil solution in a ratio of 4 mg/mL. Lastly, we added tetrabutylammonium hydroxide solution (1.5 M in H_2O, 60 μL/mL) on the ormosil solution to adjust the pH value of a sol-gel matrix.

4.2.2 Fabrication Process of a CNT-dye Hybrid Gas Sensor

Fig. 4. 1 shows a schematic diagram depicting a fabrication method for our CNT-dye hybrid gas sensor. First, small diameter CNTs (Sigma Aldrich Inc., (6; 5) chirality, ~93% semiconducting) were dispersed in a 1 mM congo red dye solution with a sonication via a tip type ultrasonicator for 1 hour. Second, 100 μL of the CNT solution was drop-casted on a PET substrate. Third, the PET substrate was heated on a hotplate to 100 ℃ for 30 min. Here, the CNTs were adsorbed on the PET substrate without coffering effect [16]. Fourth, the PET substrate was rinsed with ethanol and N,N-Dimethylformamide for 30 min, respectively. Here, the congo red molecules were removed, and only the pure CNTs remained on the PET film. Fifth, copper tapes with a conductive adhesive were attached on the PET substrate as electrodes. Lastly, a dye-functionalized sol-gel matrix was coated on the PET film via a Suslick group's method [9]. Here, we utilized methyl red or chlorophenol red to functionalize the sol-gel matrix (Sigma

Aldrich Inc.). Using this fabrication process, we successfully fabricated CNT-dye hybrid gas sensors without lithography or vacuum processes. Note that, our gas sensors were composed of flexible materials thus, the gas sensors can be bent to form versatile practical sensor devices.

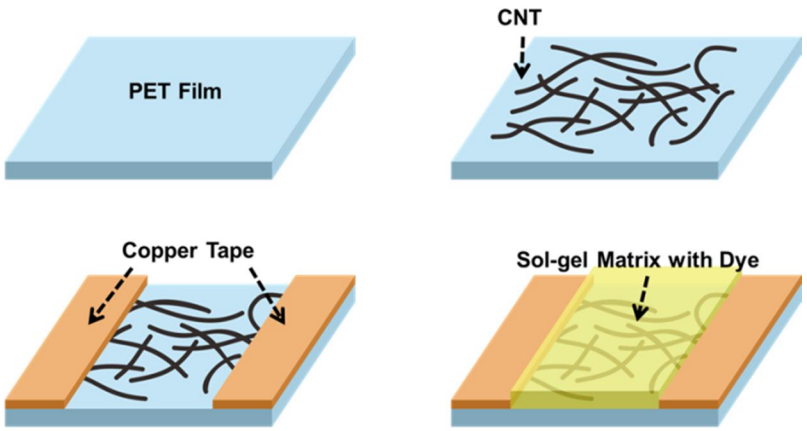

Fig. 4. 1 Schematic diagram depicting a fabrication method for our CNT-dye hybrid gas sensor. First, a PET film was coated by the CNT network via a drop-cast method. Second, electrodes were fabricated by using copper tapes. Lasty, a dye-functionalized sol-gel matrix was coated on the CNT network and cured.

4.2.3 Sensing Mechanism

Fig. 4. 2 shows the possible sensing mechanism of our CNT-dye hybrid gas sensor. When target gas molecules were absorbed on the sol-gel matrix, they reacted with water and dye in the sol-gel matrix. From the interaction, positive or negative ions are generated in the sol-gel matrix. The generated ions including hydrogen ion (H+) or hydroxide ion (OH-) changed the pH of the sol-gel matrix as well as the colour of the dye molecules in a

sol-gel matrix changed. Also, the generated ions applied the electrical potential on CNT network. Thus, the conductance of the CNT network changed [17-19].

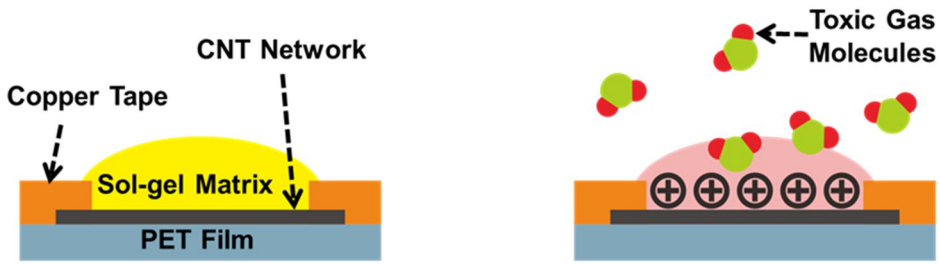

Fig. 4. 2 sensing mechanism of our CNT-dye hybrid gas sensor. When target gas was applied, the gas molecules reacted with H_2O and dye molecules in the sol-gel matrix. As a result, colours and electrical status of the colorimetric dyes were altered. Such changes were monitored by measuring the gating effect on the underlying CNT network.

4.3 Result and Discussion

4.3.1 Basic Properties of Gas Sensor

Fig. 4. 3 (a) shows the optical image of a CNT-dye hybrid gas sensor. Here, we utilized methyl red dye molecules to functionalize a sol-gel matrix and the CNT channel of the sensor was coated with the sol-gel matrix (yellow region). The size of the sensor is 2 cm x 1.5 cm. Since we utilized PET polymer films as a substrate, fabricated gas sensors are highly flexible.

Fig. 4. 3 (b) shows the AFM image of a CNT network on a PET film. The diameters of individual CNTs and CNT bundles were about 0.7 ~ 1.0 nm

and over 5 nm, respectively. Note that, we utilized small-diameter semiconducting single-walled CNTs to fabricate the CNT transistors [20]. The AFM image exhibited that CNTs were uniformly coated on the PET surface without forming bundles. This indicates that we successfully assembled CNTs on the PET film.

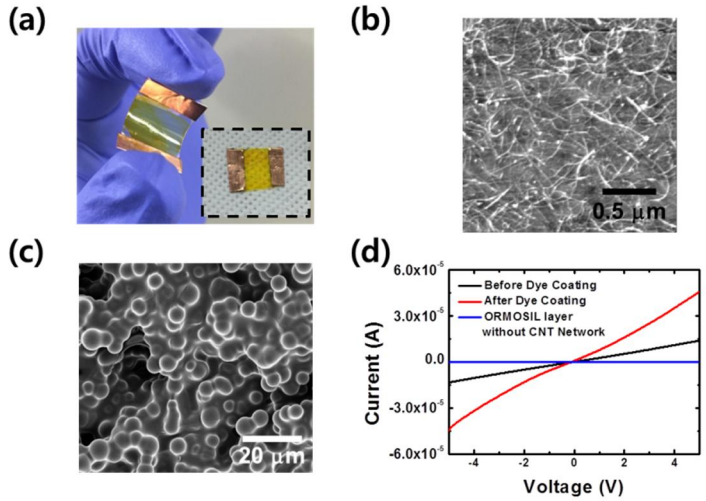

Fig. 4. 3 Basic properties of CNT-dye hybrid gas sensors. (a) Optical image of a CNT-dye hybrid gas sensor. Here, methyl red was used for the functionalization of the sol-gel matrix on the CNT channel. The CNT-dye hybrid gas sensor showed high-flexibility with high-transparency. (b) AFM topography image of CNT networks on a PET film. The CNTs were uniformly coated on the PET substrate. (c) SEM image of the surface of a sol-gel matrix. The sol-gel matrix shows a highly porous structure with a uniform silica size. (d) I-V curve of a CNT-dye hybrid gas sensor before and after the sol-gel matrix coating. The coating increased the conductance of the sensor by 2.67 times at 5 V of bias voltage.

Fig. 4. 3 (c) shows the SEM image of a sol-gel matrix surface. The sol-gel matrix shows a highly porous structure with a rather uniform silica gel size. This porous structure can hold dye-molecules and allows the

transmission of target gas molecules into our gas sensors, enabling the sensitive detection of gas molecules [21, 22].

Fig. 4. 3 (d) shows the I-V curves of a CNT-dye hybrid gas sensor before and after coating it with the sol-gel matrix. The I-V curves were measured by a semiconductor characterization system (Keithley, 4200-SCS). A bias voltage was varied from -5 V to 5 V. The conductivity of the sensor after the sol-gel matrix coating was increased about 2.67 times at 5 V. To confirm the sol-gel matrix layer is insulating, we fabricated a gas sensor without CNT network and found a negligible conductance (the blue line in Fig. 4. 3 (d)). This indicates that the sol-gel matrix was insulating, while the coating of the matrix on CNTs increased the conductivity of the CNT networks. Presumably, it is because that the sol-gel matrix on a CNT transistor changed the pH value of surrounded environment of the CNT network. It was previously reported that the change of pH value could affect the conductivity of CNT networks.

4.3.2 Selective and Refreshable Gas Sensing with a Humidity Calibration

Fig. 4. 4 (a)-i and ii show the optical images of our hybrid gas sensor before and after the SO_2 gas exposure, respectively. The size of the sample was 2 cm x 1.5 cm. Here, methyl red molecules were utilized to functionalize

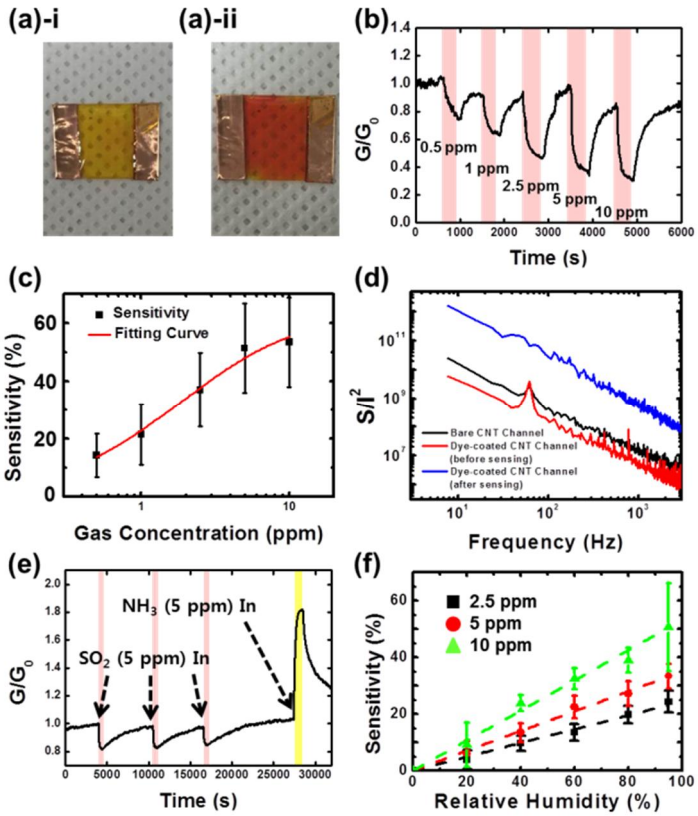

Fig. 4. 4 Selective and refreshable gas sensing with a humidity calibration. (a)-i optical image of the CNT-dye hybrid gas sensor before the gas exposure. We utilized a methyl red-functionalized CNT-dye hybrid gas sensor. The channel of the gas sensor shows yellow colour. (a)-ii optical image of the CNT-dye hybrid gas sensors after the SO_2 gas exposure. The concentration of SO_2 gas was 10 ppm. The colour of the sensor channel changed from yellow to red. (b) Real-time current measurement data obtained from a CNT-dye hybrid gas sensor after the introduction of SO_2 gases with different concentrations. We utilized a methyl red-functionalized CNT-dye hybrid gas sensor. The introduction of SO_2 caused a decrease in the conductance $\boldsymbol{G}$ of the gas sensor with respect to its original conductance value $\boldsymbol{G_0}$. (c) Sensor sensitivity ($\boldsymbol{\Delta G/G_0}$) of a CNT-dye hybrid gas sensor to various concentrations of SO_2 gas. We utilized methyl red-functionalized CNT-dye hybrid gas sensors. (d) Noise characteristics of bare CNT networks, CNT-dye hybrid gas sensor before SO_2 gas exposure and that after the exposure. We utilized a methyl red-functionalized CNT-dye hybrid gas sensor. (e) Real-time current measurement data obtained from a CNT-dye hybrid gas sensor after the introduction of SO_2 and NH_3 gases. We utilized a methyl red-functionalized CNT-dye hybrid gas sensor. (f) Sensor sensitivity ($\boldsymbol{\Delta G/G_0}$) of a CNT-dye hybrid gas sensor at various relative humidity conditions. We utilized methyl red-functionalized CNT-dye hybrid gas sensors.

a sol-gel matrix. The concentration and exposure time of the SO_2 gas was 5 ppm and 30 min, respectively. A relative humidity in the gas chamber was 95 % during the gas exposure. The colour of the sensor channel changed from yellow to red after the gas exposure, indicating the selective activation of the methyl red colorimetric dye molecules even in sol-gel matrix on CNTs.

Fig. 4. 4 (b) shows the real-time change of sensor conductance G with respect to its original value G_0 when the sensor was exposed to SO_2 gas with different concentrations. An applied bias was 0.1 V, and a relative humidity in gas chamber was 95 %. The concentration of SO_2 gas was varied from 0.5 ppm to 10 ppm. The current of the gas sensor decreased when SO_2 was applied to the gas sensor. And, the current variation increased when the concentration of the applied gas was increased. This indicates that we could estimate the concentration of the applied gas via an electrical signal. Moreover, our gas sensor showed a large conductance change of over 50% when 5 ppm of SO_2 gas (permissible exposure limit of SO_2 gas) was applied. This large conductance change could be explained by the sensing mechanism of our gas sensors. The interaction between SO_2 gas molecules and dye molecules is relying on an acid-base interaction. This acid-base interaction is much stronger than Van der Waals-type interactions between sensor surfaces and gas molecules in common semiconducting channel-based gas sensors [9, 10]. Also, a sol-gel matrix provides ions and liquid-like conditions, which

could provide an ideal environment for the gas-dye interactions and the following gating effects on the CNT transistor for a large electrical signal transduction. It also should be mentioned that the conductance of the sensor came back immediately to its original values when the target SO_2 gas was removed without any heat treatment. It clearly shows that our sensor was refreshable for repeated applications.

Fig. 4. 4 (c) shows the averaged sensor sensitivity ($\Delta G/G_0$) of CNT-dye hybrid gas sensors at various SO_2 gas concentrations. We repeated the gas sensing for more than five gas sensors to estimate average values and standard deviations. These sensor response data can be analysed by the Hill equation (red solid line in Fig. 3(c)) [24]. Here, we assumed that the sensor sensitivity ($\Delta G/G_0$) is approximately linearly proportional to the surface density C_s of gas molecules adsorbed on dye molecules. Then, the sensor sensitivity can be written like

$$\frac{\Delta G}{G_0} \sim kC_s = k\,\frac{C_{s,max}\cdot C^n}{{K_d}^n + C^n}$$

where k, $C_{s,max}$, n, C and K_d are a sensor response coefficient, maximum surface gas density, Hill coefficient, concentration of SO_2 gas and dissociation constant, respectively. From the fitting curve, the Hill coefficient and dissociation constant were estimated as 1.028 and 0.919 x 10^{-7} M,

respectively. The estimated dissociation constant is similar with a reported value of the case when the gas molecules bind to dye molecules in water at 25 ℃ [25]. We also could estimate the theoretical dissociation constant in our CNT-dye hybrid gas sensor structures. In brief, the dissociation constant in our device structures was estimated by multiplying a dissociation constant of SO_2 acid hydrolysis reaction and a dissociation constant of methyl red dye. The theoretical dissociation constant of our gas sensor $K_{d\text{-}theo}$ is given by 1.03 x 10^{-7} M. The theoretical $K_{d\text{-}theo}$ value is similar with our experimental value of K_d. The estimated Hill coefficient is close to 1, indicating that the affinity of the SO_2 molecules for binding sites was not dependent on other SO_2 molecules bound on the sensor. These results show that our sensors can be used for the reliable quantitative analysis of gas species based on the sensor signals.

Fig. 4. 4 (d) shows the noise characteristics of a bare CNT channel and a sol-gel matrix-coated CNT channel (before and after the exposure to 10 ppm SO_2). The noise characteristics are measured using a fast Fourier-transform network analyser (SR 770). The 4 V of bias voltage was applied on the gas sensor for all noise measurements. The bare CNT network and our sensors exhibited a typical $1/f$ noise behaviour [26, 27]. Interestingly, the noise power density of the gas sensor was increased significantly after gas

sensing, indicating that the sol-gel matrix, when exposed to SO_2 gas, could act as a noise source. Presumably, when the SO_2 gas binds to dye molecules, the number of positive ions in sol-gel matrix was increased and such positive ions could work as charge traps in the channel [28].

Fig. 4. 4 (e) shows the real-time responses of our sensors to SO_2 and NH_3 gases. The sensing graph was measured at 0.1 V of bias voltage and 95 % of relative humidity. SO_2 gas (5 ppm) was applied during 500 seconds at intervals of about 6500 seconds (pink region). Subsequently, NH_3 gas (5 ppm) was applied during 500 seconds (yellow region). Note that the conductance of the gas sensor decreased during the repeated exposures of the SO_2 gas, indicating our gas sensor is reusable without any heat treatment. Interestingly, the conductance of the gas sensor increased when the sensor was exposed to NH_3 gas. In previous researches, the conductance of bare CNT-based gas sensors decreased when NH_3 gas was applied [29, 30]. However, our gas sensor exhibited an opposite behaviour, showing that the response of our sensors came mainly from a reaction between gas and dye molecules in a sol-gel matrix. These results support that we can build different selectively gas sensors simply by using different dyes in the sol-gel matrix [9, 10]. We fabricated CNT-dye hybrid gas sensors by functionalizing the methyl red and chlorophenol red dyes in the sol-gel matrix. Using the methyl red and chlorophenol red-functionalized gas sensors, we successfully discriminated

SO_2, NH_3 and Cl_2 gases.

Fig. 4. 4 (f) shows the sensitivity of our gas sensors at different relative humidity conditions. Here, the relative humidity was varied from 0 % to 95 %. The concentrations of the exposed SO_2 gas were 2.5, 5 and 10 ppm, and the numbers of measured gas sensors were over seven for each data point. The gas sensors exhibited no responses at a zero relative humidity, and the response linearly increased as the relative humidity increased. Previous works using electrochemical sensors show that when a relative humidity increased, the thickness of a water layer on a sol-gel matrix increased, and, as a result, the amount of dissolved SO_2 gas and resulting sensor signals also increased [9, 10, 31]. Note that, some CNT based gas sensors in previous researches showed a linear humidity dependence [32, 33]. Such a linear humidity dependence can be a significant advantage of our sensors, which enables rather simple calibration of the sensing signals for the quantitative measurement of gas concentration. For an example, the sensitivity of the gas sensors at 10 ppm of SO_2 gas was given by

$$\frac{\Delta G}{G_0} = 0.53 \cdot RH \qquad (0 \leqq RH \leqq 1)$$

where RH is a relative humidity.

4.3.3 Tube-Shape Gas Sensors based on Folded CNT Sensors

Since our gas sensors were fabricated with only flexible materials such as a PET film, copper tapes and CNTs, we could easily bend it to build tube-shape gas sensors. Fig. 4. 5 (a) shows the photographic image of a tube-shape CNT-dye hybrid gas sensor. The height, channel length and radius of the gas sensor are 20, 10 and 2.5 mm, respectively. Fig. 4. 5 (b) shows the photographic image of the gas sensor after SO2 (10 ppm) exposure. The colour of the sensor channel was changed from yellow to red, indicating that dye molecules in a sol-gel matrix still maintained its activity even under a highly-bent condition.

Fig. 4. 5 (c) and (d) show the I-V curves and noise characteristics of a CNT-dye hybrid gas sensor before and after bending. The noise characteristics were measured using a fast Fourier-transform network analyser (SR 770). The 4 V of bias voltage was applied on the gas sensor during the noise measurement. Note that the I-V characteristics of the CNT-dye hybrid gas sensor did not change much even when the sensor was bent into a tube shape. The noise characteristics of the gas sensor exhibited a typical 1/*f* behaviour, and it did not change much when the sensor was bent. This implies that our sensors can operate under a highly-bent condition.

Fig. 4. 5 (e) shows the real-time electrical measurment of SO_2 gas from a tube-shape CNT-dye hybrid gas sensor. An applied bias was 0.1V, and a relative humidity was maintained at 95% during the measurement. The SO_2 gas (10 ppm) was applied for 400s at the intervals of 1000s. The conductance of the gas sensor decreased by 70% at the gas exposure, while it was recovered back when the gas chamber was vented at each process. This result implies that our tube-shape sensors operated properly, and our flexible gas sensors can be used for versatile applications requiring highly-bent devices.

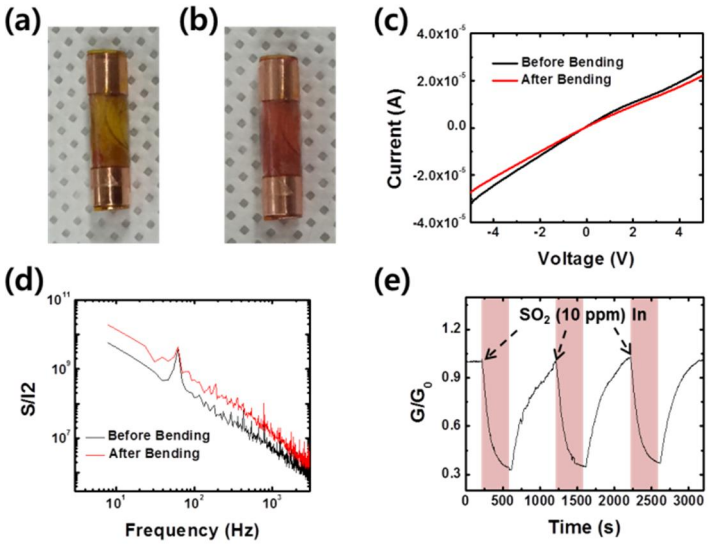

Fig. 4. 5 Tube-shape gas sensors based on folded CNT sensors. We utilized methyl red-functionalized gas sensors. (a) Optical image of tube-shape CNT-dye hybrid gas sensor before the gas exposure. (b) Optical image of tube-shape CNT-dye hybrid gas sensor after the SO_2 gas exposure. The colour of the sensor channel was clearly changed yellow to red. (c) I-V curve of the CNT-dye hybrid gas sensor before and during the bending. (d) Noise characteristics of the CNT-dye hybrid gas sensor before and during the bending. (e) Real-time current measurement data obtained from bent CNT-dye hybrid gas sensor after the introduction of SO_2 (10 ppm).

4.5 Summary

We have developed a highly-flexible and refreshable CNT-dye hybrid gas sensor for the selective and sensitive gas sensing. The CNT-dye hybrid structure was fabricated by coating the colorimetric dye-functionalized sol-gel matrix layer on a CNT network. The CNT-dye hybrid gas sensor with different dye species could be used to detect versatile gas species such as SO_2, NH_3 and Cl_2 with a high-sensitivity and selectivity. Also, the conductance of the CNT-dye hybrid gas sensors was easily recovered back to its original without any heat treatment when target gas molecules were removed. The sensitivity of the gas sensor exhibited linear dependence to relative humidity, enabling easy calibration of our sensor for quantitative analysis of gas species. Furthermore, our sensors can be easily bent into different shapes for versatile device applications such as tube-shape gas sensors. This work provides a simple but quite versatile strategy to build highly flexible and refreshable gas sensors and can be utilized for various practical applications such as monitoring hazardous gas species in industrial complexes.

References

[1] F. K. Perkins et al., Chemical Vapor Sensing with Mono layer MoS_2. *Nano Lett.* **13**, 668-673 (2013).

[2] S. Rumyantsev, G. X. Liu, M. S. Shur, R. A. Potyrailo, A. A. Balandin, Selective Gas Sensing with a Single Pristine Graphene Transistor. *Nano Lett.* **12**, 2294-2298 (2012).

[3] C. W. Na, H. S. Woo, I. D. Kim, J. H. Lee, Selective detection of NO2 and C_2H_5OH using a Co_3O_4-decorated ZnO nanowire network sensor. *Chem. Commun.* **47**, 5148-5150 (2011).

[4] A. Star, V. Joshi, S. Skarupo, D. Thomas, J. C. P. Gabriel, Gas sensor array based on metal-decorated carbon nanotubes. *J. Phys. Chem. B* **110**, 21014-21020 (2006).

[5] J. F. Liu, X. Wang, Q. Peng, Y. D. Li, Vanadium pentoxide nanobelts: Highly selective and stable ethanol sensor materials. *Adv. Mater.* **17**, 764-767 (2005).

[6] M. Asad, M. H. Sheikhi, M. Pourfath, M. Moradid, High sensitive and selective flexible H2S gas sensors based on Cu nanoparticle decorated SWCNTs. *Sensor. Actuat. B: Chem.* **210**, 1-8 (2015).

[7] B. Wang, J. C. Cancilla, J. S. Torrecilla, H. Haick, Artificial Sensing Intelligence with Silicon Nanowires for Ultraselective Detection in the Gas Phase. *Nano Lett.* **14**, 933-938 (2014).

[8] H. Y. Jeong et al., Flexible room-temperature NO_2 gas sensors based on carbon nanotubes/reduced graphene hybrid films. *Appl. Phys. Lett.* **96**, 213105 (2010).

[9] L. A. Feng et al., Colorimetric Sensor Array for Determination and Identification of Toxic Industrial Chemicals. *Anal. Chem.* **82**, 9433-9440 (2010).

[10] M. C. Janzen, J. B. Ponder, D. P. Bailey, C. K. Ingison, K. S. Suslick, Colorimetric sensor Arrays for volatile organic compounds. *Anal. Chem.* **78**, 3591-3600 (2006).

[11] S. H. Lim, L. Feng, J. W. Kemling, C. J. Musto, K. S. Suslick, An optoelectronic nose for the detection of toxic gases. *Nat. Chem.* **1**, 562-567 (2009).

[12] N. A. Rakow, K. S. Suslick, A colorimetric sensor array for odour visualization. *Nature* **406**, 710-713 (2000).

[13] N. Dossi et al., An electrochemical gas sensor based on paper supported room temperature ionic liquids. *Lab. Chip.* **12**, 153-158 (2012).

[14] V. V. Plashnitsa, P. Elumalai, Y. Fujio, N. Miura, Zirconia-based electrochemical gas

sensors using nano-structured sensing materials aiming at detection of automotive exhausts. *Electrochim. Acta* **54**, 6099-6106 (2009).

[15] M. Breedon, N. Miura, Augmenting H-2 sensing performance of YSZ-based electrochemical gas sensors via the application of Au mesh and YSZ coating. *Sensor. Actuat. B: Chem.* **182**, 40-44 (2013).

[16] A. K. Sundramoorthy, Y. C. Wang, S. Gunasekaran, Low-temperature solution process for preparing flexible transparent carbon nanotube film for use in flexible supercapacitors. *Nano Res.* **8**, 3430-3445 (2015).

[17] C. Rottman, A. Turniansky, D. Avnir, Sol-gel physical and covalent entrapment of three methyl red indicators: A comparative study. *J. Sol-Gel Sci. Techn.* **13**, 17-25 (1998).

[18] B. Kim et al., Highly selective and sensitive detection of neurotransmitters using receptor-modified single-walled carbon nanotube sensors. *Nanotechnology* **24**, 285501 (2013).

[19] D. Son et al., Nanoneedle Transistor-Based Sensors for the Selective Detection of Intracellular Calcium Ions. *Acs Nano* **5**, 3888-3895 (2011).

[20] A. A. Green, M. C. Hersam, Nearly Single-Chirality Single-Walled Carbon Nanotubes Produced via Orthogonal Iterative Density Gradient Ultracentrifugation. *Adv. Mater.* **23**, 2185-2190 (2011).

[21] J. Zhang, J. Guo, H. Y. Xu, B. Q. Cao, Reactive-Template Fabrication of Porous SnO2 Nanotubes and Their Remarkable Gas-Sensing Performance. *ACS Appl. Mater. Inter.* **5**, 7893-7898 (2013).

[22] X. B. Li et al., Porous spheres-like ZnO nanostructure as sensitive gas sensors for acetone detection. *Mater. Lett.* **100**, 119-123 (2013).

[23] J. Lee et al., Floating electrode transistor based on purified semiconducting carbon nanotubes for high source-drain voltage operation. *Nanotechnology* **23**, 085204 (2012).

[24] M. Lee et al., 100 nm scale low-noise sensors based on aligned carbon nanotube networks: overcoming the fundamental limitation of network-based sensors. *Nanotechnology* **21**, 055504 (2010).

[25] C. S. Chang, G. T. Rochelle, So2 Absorption into Aqueous-Solutions. *AIChE J.* **27**, 292-298 (1981).

[26] S. Soliveres, J. Gyani, C. Delseny, A. Hoffmann, F. Pascal, 1/f noise and percolation in

carbon nanotube random networks. *Appl. Phys. Lett.* **90**, 082107 (2007).

[27] J. Kim et al., Large Scale Assembly of Pristine Semiconducting Carbon Nanotube Network-Based Devices Exhibiting Intrinsic Characteristics. *J. Phys. Chem. C* **117**, 19721-19728 (2013).

[28] J. Chermiti, S. Azzouzi, M. B. Ali, M. Trabelsi, Modeling and Analysis of Low Frequency Noise in Ion Field-Effect Transistors Sensors. *MNSMS.* **4**, 119-127 (2014).

[29] J. Kong et al., Nanotube molecular wires as chemical sensors. *Science* **287**, 622-625 (2000).

[30] F. Rigoni et al., Enhancing the sensitivity of chemiresistor gas sensors based on pristine carbon nanotubes to detect low-ppb ammonia concentrations in the environment. *Analyst* **138**, 7392-7399 (2013).

[31] J. Hu, X. D. Xiao, D. F. Ogletree, M. Salmeron, Imaging the Condensation and Evaporation of Molecularly Thin-Films of Water with Nanometer Resolution. *Science* **268**, 267-269 (1995).

[32] T. Zhang et al., Poly(m-aminobenzene sulfonic acid) functionalized single-walled carbon nanotubes based gas sensor. *Nanotechnology* **18**, 165504 (2007).

[33] G. P. Evans et al., Controlling the Cross-Sensitivity of Carbon Nanotube-Based Gas Sensors to Water Using Zeolites. *ACS Appl. Mater. Inter.* **8**, 28096-28104 (2016).

Chapter 5.

Conclusion

In this dissertation, first, we discussed a method for the large scale assembly of pristine s-CNT network-based devices without bundles or organic impurities. in this method, we fabricated pristine s-CNT network-based FETs via a centrifugation method and a filteration method, the fabricated FETs showed an improved on−off ratio up to over $\sim 10^6$ and a subthreshold swing value down to $\sim$490 mV/dec. Interestingly, we observed a saturation behavior of a drain-source current of our pristine s-CNT-network based FET at a large negative gate bias. Such improved performance and anomalous saturation behavior were attributed to the uniform threshold voltage of our pristine s-CNT networks.

Secondly, we measured the noise map of sorted CNT networks via a "noise spectral imaging" method. In this discussion, we measured current maps and current-noise PSD maps of sorted CNT networks via a spectrum analyzer-functionalized conducting AFM. Then we calculated conductivity maps, mobility maps, scaling factor maps and noise source density maps via the measured maps. The experimental result exhibited that the noise activity

of a CNT network was depending on the density of a CNT network and diameters of CNTs. Also, we found that a large amount of noise occurs at crossed CNT-CNT junctions in the case of a semiconducting CNT network. Additionally, we compared the noise characteristics of sorted CNTs by measuring a cross-patterned CNT network of a metallic CNT networks and a semiconducting CNT networks.

Lastly, we discussed a CNT-dye hybrid gas sensor for the selective and sensitive gas sensing. We coated dye molecules on s-CNT networks via sol-gel method to fabricate the CNT-dye hybrid structure. Using the gas sensors, we detected SO_2 gas via optical and electrical signals. Our gas sensor showed high sensitivity of more than 50%. Also, our gas sensors were easily recovered back to its original without any heat treatment by venting on N_2 gas. The sensitivity of the gas sensor showed linear dependence to relative humidity, enabling easy analysis of sensing data. Furthermore, we fabricated tube-shaped CNT-dye hybrid gas sensors for versatile device applications.

Since our works reveal valuable insights about the characteristics of sorted CNT networks, it can be an important guide line for the application about future high-performance sorted CNT-based devices.

Chapter 6.

Abstract in Korean

초록

분리된 탄소나노튜브의 전기적 성질과 이를 이용한 가스센서 개발에 관한 연구

김정수

물리천문학부

서울대학교 대학원

탄소나노튜브는 높은 전류밀도, 높은 on-off 전류비, 높은 전자 이동도, 낮은 subthreshold swing 등과 같은 우수한 전기적 성질을 가지고 있어 차세대 전자공학 연구를 위한 핵심 물질로 기대 받고 있다. 하지만, 탄소나노튜브를 이용한 나노소자의 개발은 그 제작방법이 복잡하고, 시간이 많이 걸려서 상용화 하는데 많은 어려움을 겪고 있다. 예를 들어 막 성장된 탄소나노튜브는 cirality가 임의로 결정되는 특징을 가지고 있다. 따라서 막 성장된 탄소나토뷰는 금속성 탄소나노튜브와 반도체성 탄소나노튜브가 혼합되어 있게 된다. 금속성 탄소나노튜브와 반도체성 탄소나노튜브는 서로 반대의 전기적 성질을 가지고 있기 때문에, 이러한 탄소나노튜브가 모두 포함되어 있는 막 성장된 탄소나노튜브를 이용하여 소자를 제작할 경우 우수한 성능을 기대하기 힘들게 된다. 최근 이러한 문

제를 해결하기 위하여 “density gradient ultracentrifugation (DGU)” 방법이 개발되어 막 성장된 탄소나노튜브에서 금속성 탄소나노튜브와 반도체성 탄소나노튜브를 분리하는데 성공하였다. 하지만, 효과적인 제작방법의 부재로 인해 분리된 탄소나노튜브의 전기적 성질 조시 및 상용화에 관한 연구가 아직 진행 중에 있다.

본 논문에서는 분리된 탄소나노튜브의 전기적 성질을 다양한 방법으로 조사하였으며, 이러한 연구를 바탕으로 탄소나노튜브를 가스센서로 활용하는 방법에 관하여 논의할 예정이다.

그에 대한 첫 번째 내용으로, 단일 탄소나노튜브의 성능을 보이는 순수 반도체성 탄소나노튜브 네트워크 기반 소자제작방법에 관하여 하여 언급할 것이다. 일반적인 분리된 탄소나노튜브 네트워크 기반 소자는 소자의 채널부분에 계면활성제 또는 탄소나노튜브 번들이 존재한다는 단점을 가지고 있다. 이러한 번들 혹은 계면활성제는 소자의 성능을 낮추지만 둘을 동시에 제거하기가 극도로 어렵기 때문에 고성능 소자를 제작하는데 어려움으로 작용하고 있다. 본 논문에서 저자들은 원심분리법과 막여과기법을 이용하여 탄소나노튜브 번들과 유기불순물이 없는 순수 반도체성 탄소나노튜브 용액을 제작하였다. 이렇게 제작된 탄소나노튜브 용액을 이용하여 순수 반도체성 탄소나노튜브 네트워크 기반 소자를 제작하였으며, 그 성능을 측정하였다. 그 결과 on-off 전류비는 10^6에 육박하며, subthreshold swing은 490 mV/dec의 낮은 값을 보여서 단일 탄소나노튜브를 이용해 만든 소자에 육박한 성능을 보였다.

다음으로 주사 잡음 현미경을 이용한 분리된 탄소나노튜브의 전류 잡음 특성 측정에 관하여 논의할 것이다. 여기서, 저자들은 반도체성 탄소나노튜브 네트워크와 금속성 탄소나노튜브 네트워크의 2차원 전류 이미지와 2차원 잡음 스펙트럴 파워 밀도 이미지를 개조된 전도성 주사탐침현미경을 이용하여 측정하였다. 측정된 2차원 전류 이미지와 2차원 잡

음 스펙트럴 파워 밀도 이미지를 이용하여, 분리된 탄소나노튜브 네트워크들의 전류 잡음 소스의 활동성을 분석하였다. 그 결과, 전류 잡음 소스의 활동성은 탄소나노튜브 네트워크의 밀도와, 탄소나노튜브의 두께에 의존한다는 것을 발견하였다. 또한 반도체성 탄소나노튜브의 경우 전류 잡음 소스의 활동성이 탄소나노튜브들이 교차된 지점에서 높게 나온다는 것을 확인하였다.

마지막으로, 발색시약이 기능화된 졸-겔 매트릭스와 반도체성 탄소나노튜브의 복합구조를 이용하여 듀얼-모드 검지가 가능한 가스센서 개발에 관하여 논의할 것이다. 여기서 자저는 졸-겔 법을 이용하여 반도체성 탄소나노튜브위에 발색시약을 코팅하여 탄소나노튜브-발색시약 복합구조 가스센서를 제작하였다. 제작된 가스센서를 이용하여 SO_2, NH_3, CL_2 가스를 광학적, 전기적 신호로 검지 하였으며, 이 신호를 토대로 가스의 종류를 구분할 수 있었다. 개발된 가스센서의 민감도는 배출 허용 기준치 이하의 가스 농도에서도 50 % 이상의 고 민감도를 보였다. 또한 반도체성 탄소나노튜브-발색시약 복합구조 가스센서의 경우 N2 가스에 노출함으로써 쉽게 재사용 가능한 상태로 만들 수 있었다.

본 연구는 분리된 탄소나노튜브의 전기적 성질에 대한 중요한 정보를 제공하고, 이를 이용한 실질적인 응용에 대한 가이드라인이 될 수 있다.

주요어: 탄소나노튜브, 트랜지스터, 원심분리법, 주사탐침현미경, 저주파 전류 잡음, 전류 잡음 이미징, 발색시약 센서, 가스 센서

학번: 2013-30112